Fast retuning of superconducting radiofrequency accelerating cavities in the

European Spallation Source linear accelerator

SOFIA JOHANNESSON
MASTER'S THESIS
DEPARTMENT OF ELECTRICAL AND INFORMATION TECHNOLOGY
FACULTY OF ENGINEERING | LTH | LUND UNIVERSITY
IN COOPERATION WITH ESS

Fast retuning of superconducting radiofrequency accelerating cavities in the European Spallation Source linear accelerator.

Sofia Johannesson

May 2020

Thesis submitted for degree Master of Science in Engineering, Engineering Physics.

Supervised by Dr. Yngve Levinsen[1] and Prof. Anders Karlsson[2].

---

[1]European Spallation Source ERIC, Lund, Sweden
[2]Department of Electrical and Information Technology, Lund University, Lund, Sweden

Abstract

The aim of the degree project is to continue the work of PhD student YuanShuai Qin on creating a fast retuning of the ESS accelerator lattice in the event of an accelerating cavity being offline. The main goal of the project was evaluating and improving the retuning routine created my YuanShuai Qin. The major concern is to maintain beam stability by reducing emittance growth and keeping the beam phase advance smooth.

Firstly, the original Matlab code for retuning authored by YuanShuai Qin was translated to python. This work included creating a genetic algorithm used as the optimizer on the retuning process. To make sure that this had been done correctly, the transfer matrix of a small lattice containing a few cavities were compared between TraceWin, the original Matlab code and the new python code. The resulting transfer matrix of the Pyhton code was closer to TraceWin than the transfer matrix calculated from the original Matlab script.

One of the major approximations used in the retuning routine was the exclusion of space charge effects. To determine if this was a too crude approximation a new lattice was created, which is the ESS lattice but matched without the effects of space charge. The Twiss parameter β was accurately calculated, with TraceWin as reference, when space charge was not considered in the simulations but not when the effects were included.

However, the matching routine was tested on both lattices for failed cavities at different positions in the accelerator. The main conclusion was that the beam stability was maintained only slightly better when the effects of space charge was excluded compared to the effects were included. One of the major issues, including or excluding space charge effects, was an increasing beam phase advance for the retuned lattices. This was attempted to be rectified using beam phase advance optimization in the fitness function fed to the genetic algorithm used for the retuning process. This new fitness function made the retuning extremely slow and did not improve the resulting lattice much. Therefore, the conclusion is that if the retuning routine is to be improved, space charge should be included in the optimization, perhaps by creating the transfer matrices with respect to the effects of space charge.

Acknowledgements

Contents

1 Introduction

Neutron sources are used to investigate properties of biological and physical matter. They are useful in multiple scientific disciplines and are therefore in high demand. In 2003 it was decided by ESFRI (European Strategy Forum for Research Infrastructure) that a spallation source with a single target producing a 5 MW beam would be built to meet the high demand for a neutron source. A few years later, in 2009, it was decided that the new neutron source was to be built in Lund, Sweden. The construction of the European Spallation Source (ESS) started in 2013 and the facility is expected to be fully operational in 2025. [1]

ESS is designed to have a time-average flux of neutrons comparable to existing continuous neutron sources such as the Institut Laue-Langevin (ILL). This is done by using a beam power of 5 MW. In addition, loss of efficiency is avoided, even for the slowest neutrons produced, by having a low enough pulse repetition rate. This means that the energy per pulse is 357 kJ. To achieve this energy per pulse, each proton needs to have an energy of a few GeVs. The ESS linac is therefore accelerating protons to 2 GeV before hitting a rotating tungsten target. [1]

This degree project has been conducted with the Beam Physics Section at the Accelerator Division in ESS and concerns the operation of the linac. The linac at ESS is 600 m long, providing a 2.86 ms long beam pulse at 14 Hz, with a peak proton current of 62.5 mA. The protons are accelerated using mainly 146 superconducting RF cavities. These are split into three families where 26 cavities are spokes, 36 are medium-beta elliptical and 84 are high-beta elliptical cavities. For this degree project they are all assumed to have axially symmetrical electromagnetic field. The powering system of a RF accelerating cavity is complex and can malfunction, as an example one of the klystrons powering the cavity can go offline. If the powering system fails, a cavity can be offline for everything between hours to months. To ensure beam availability it is necessary to quickly retuning the still online cavities to compensate for the offline ones. This retuning process needs to keep beam dynamics stable to recommence the neutron production.

2 The linac

2.1 Short description of the ESS linac

ESS consists of three main components; a linear accelerator that accelerates protons, a target and 22 instruments that utilize the neutron beam for materials research. The neutrons are produces through spallation as the 2 GeV proton beam hits a metal target destabilizing the atoms. Spallation is the process knocking out particles from a nucleus using smaller particles. The produced neutrons inherit the pulsed time structure of the proton beam when it hits the rotating tungsten target. [1]

The two main goals of the ESS are to deliver a time averaged flux of neutrons comparable to the currently most intense continuous source (ILL) and have pulse repetition rate low enough to avoid loss of efficiency in the use of high flux neutron. The loss of efficiency should be low for neutrons of all temperatures. These requirements lead to an average beam power of 5 MW and 357 kJ of energy per pulse. A neutron-beam with these specifications can be produced by a proton beam, each having an energy of a few GeV. [1]

This degree project focuses on operation the linac, and in particular the operation of the superconducting cavities. Each component of the linac is presented in figure 1. Each section is briefly described below.
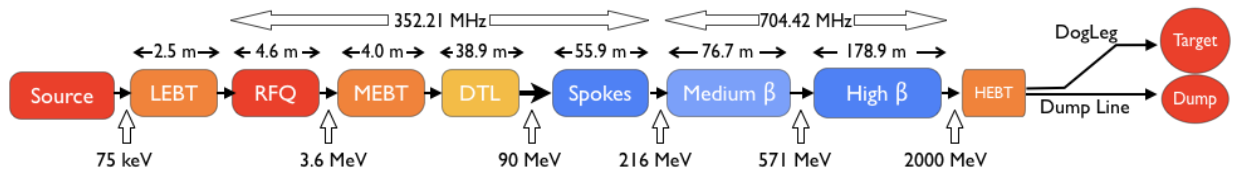

Figure 1: This is a summary of the ESS linac. A red, orange or yellow box indicates that the section is normal conducting whereas a blue box indicates that the section is superconducting. The figure also indicates the beam energy at different positions in the linac as well as the RF frequency.

Source The ion source is a pulsed microwave-discharge ion source (MDIS) on a platform of 75 kV. This device produced a beam of 75 keV with a current of 62.5 mA. [1]

LEBT (Low Energy Beam Transport) focuses the beam to the entrance of the RFQ using two solenoid magnets. It also contains beam diagnostics (instruments for measuring beam characteristics) and a chopper to produce the pulsed beam structure required by RFQ. [1]

RFQ (Radio Frequency Quadrupole) is a device that both amplifies the bunching of the beam at 352.21 MHz and accelerates the beam to 3.6 MeV. It is specifically designed for ESS to have small losses and minimal emittance growth. The RFQ is powered by a 3 MW klystron at 352.21 MHz, which is the frequency of the warm part linac and the spoke cavities. [1] [2]

MEBT (Medium Energy Beam Transport) transports and focuses the beam from the RFQ to the entrance of the DTL using three buncher cavities and eleven quadrupoles. In addition, it contains elements for beam instrumentation and a chopper that is faster than the LEBT chopper. [1]

DTL (Drift Tube Linac) follows the MEBT and is the last part of the normal conducting linac. The DTL accelerates the beam from 3.6 MeV to 90 MeV and has a FODO structure. A FODO structure keeps the beam stable transversally by focusing and defocusing the beam periodically, which is done using quadrupoles. Furthermore, the DTL contains beam position monitors (BPMs). [1] The DTL has 5 tanks and is transversally focused using permanent magnet quadrupoles. [3]

SPK (superconducting double-spoke cavities) are the first family of accelerating superconducting cavities used and has an optimum beta value of 0.5. The proton beam gains 95 % of its final energy from the superconducting part, however just 20% of the phase advance, the rest is previously acquired in the normal conducting part of the linac. The ESS linac has 26 spokes divided over 13 cryomodules. The SPK cavities operate with a frequency of 352.21 MHz previously mentioned, see also [1]. The SPK cavities will be powered by 200 kW tetrodes, see [4].

Medium β and High β or simply **MBL** and **HBL** are the second and third families of superconducting accelerating cavities used in the ESS linac. They are elliptical cavities with a geometrical beta of 0.67 respectively 0.86. They have the same length with leads to a 6-cell MBL and a 5-cell HBL. Because the MBL and HBL cavities are the same length, the cryomodule design can be similar for both types. The cryomodules here house four cavities each. There are in total 36 MBLs and 84 HBLs that all operate with an RF frequency of 704.42, which is twice as much in as the previous sections of the linac. This means that every second RF bucket will contain a bunch since the beam is still bunched at 352.21 MHz. Between the cryomodules are warm quadrupoles placed to keep the beam focused. Also BPM's, steering magnets and beam instrumentation devices are placed in these LWU's (linac warm units). The surface field gradient of the MBL and HBL cavities is 45 MV m^{-1}, which is higher than any other cavity field gradient. The beam energy at the end of the HBLs is 2 GeV, which is the final beam energy. [1] The MBL cavities will be powered by 1.5 MW klystrons and the HBL cavities will be powered by IOTs (inductive output tubes). In case IOTs will not be availabe in time, also the HBL cavities will be powered by 1.5 MW klystrons, see [4].

HEBT (high energy beam transport) transports the beam from the HBL to the first dipole. This is referred to as the contingency area, which means that it is an area dedicated to potential additional cavities. [2]

A2T (Accelerator to target) transports the beam from the HEBT to the target using dipole magnets to first steer the beam 4° upwards to reach ground level and then 4° downwards to again be parallel to the ground. In addition to steering the beam to the target, the A2T makes the beam profile quasi-rectangular before hitting the target. A rastering system consisting of 8 magnets paints the target with the beam in different horizontal and vertical frequencies, see [5].

Beam Dump is located in line of sight of the linac, thus underneath the target, and is able to absorb 12.5 kW of beam power. The first dipole in A2T acts as a switching magnet between the target and the beam dump. [5]

All in all, the linac is 600 m long, where 300 m consists of the superconducting cavities. It is in an underground tunnel covered by five meters of soil for radiation protection. [1]

2.2 Accelerator elements

In this project three elements of the accelerator have been used for the calculations. These elements are drift spaces, quadrupoles and RF cavities. Below is a description for each element including a derivation of the 6D transfer matrices acting on the 6D particle coordinates $[x, x', y, y', z, \delta]$. In this degree project it is assumed that all off-diagonal 2D elements are zero, meaning no magnetic misalignment or skew quadrupoles.

A 2D phase space is the plane consisting of the axis x and the axis x', where x' is derivative $\frac{dx}{ds}$. These two coordinates correspond to the position and angle of the particle in one dimension. This is a useful way of describing a beam since Twiss parameters can be used connects single particle tracking of ions to the wider view of beam envelopes. Every particle in the beam can be drawn in the phase space. The ellipse that encircles most, usually 95%, of these particles is called the phase ellipse. The phase ellipse can then be described by the Twiss parameters according to figure 2. The emittance is invariant, which will be

further addressed in section 2.3. Separating the beam size in the emittance and the Twiss parameters is convenient as the emittance describes the area and the Twiss parameters describes the shape of the phase space ellipse. [6]
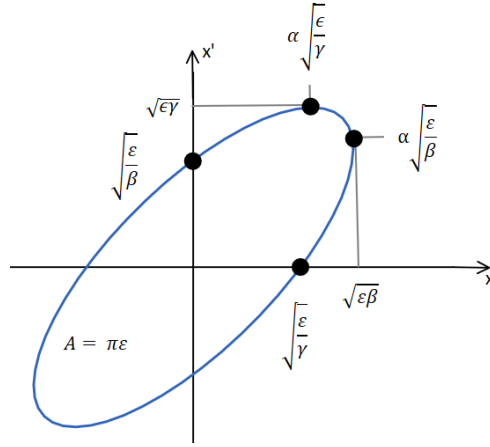

Figure 2: The figure shows an example of the phase ellipse in the phase space xx'. The area of the ellipse can be described by the emittance, ϵ, and the shape by the three Twiss parameters: α, β and γ.

The 6D phase space in this thesis is defined by the position and momentum in relation to the synchronous particle in each dimension. The field a particle experiences travelling through a RF cavity can be described as the blue curve in figure 3. Note that the x-axis is the input phase of the particle. The particle performs synchronous oscillations in the stable region marked by the two outer points. The center point of this region is called the synchronous phase, a particle with this phase does not oscillate but will stay in the same place on this curve, and in the 2D phase space. [7]
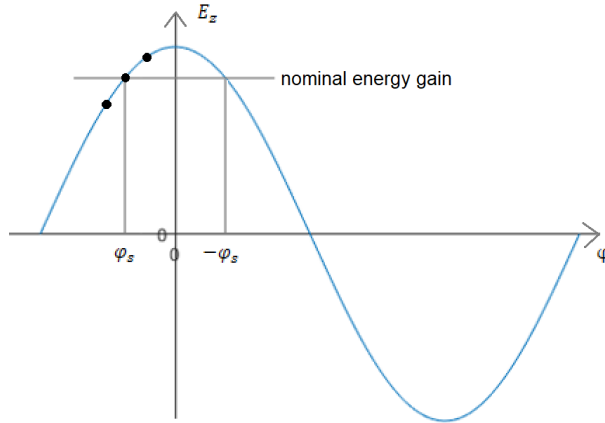
Figure 3: The figure shows the acceleration of a particle in an RF gap as a function of its phase. The stable region and the synchronous phase is marked with dots representing a possible particle positing.

The longitudinal phase space can be described by $\Delta W, \Delta\varphi$ where ΔW is the energy the particle gains in a cavity [7]. The phase can also be connected to the momentum of the particle. If a particle has $\varphi > \varphi_s$, it will gain more energy, have a higher momentum $p > p_s$ and will therefore arrive early at the next cavity. Then the phase will be larger $\varphi < \varphi_s$. This is the synchronous oscillations. Due to this connection, alternative dimensions of the phase space is z, δ where $z = -\frac{\varphi}{2\pi} \cdot \beta\lambda$ and $\delta = \frac{p - p_s}{p_s}$. The momentum of the particle is related to the change in phase. [8]

4

Figure 4: The image shows a particle moving in the xz-plane of a drift space of length L.

2.2.1 Drift space

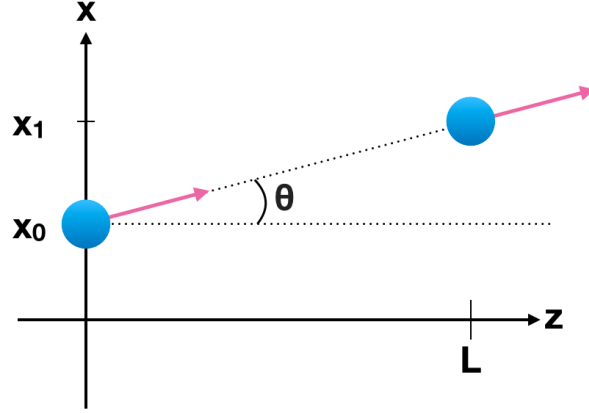An accelerator space without any magnetic elements is called a drift space [9]. To derive the transfer matrices for the transverse measurables $[x, x', y, y']$ one does not need to take relativistic effects into account. Figure 4 shows how the particle moves in the xz-plane in a drift space. Two positions of the particle is depicted in the image, the first being the particles position at the entrance of the drift space, see x_0, and the second is the position of the particle in this plane at the exit if a drift space, see x_1. The length of the drift space is L. The angle, θ will remain unchanged throughout the entire drift space, whereas the x-coordinate will change from x_0 to x_1. This change can be described by equation (1), note that $\tan(\theta) = \frac{x_1 - x_0}{L} = \frac{\Delta x}{\Delta z} \approx \frac{\partial x}{\partial z} = x'$ which for small angles means that $\theta \approx x'$, since $\tan(\theta) \approx \theta$ if θ is small. The transfer matrix is given by $\mathbf{T}_{\text{Drift,x}}$. [10]

$$
\begin{array}{ll}
x_1 = & x_0 \quad + L \cdot \theta = x_0 + L \cdot x' \\
x_1' = & x_0'
\end{array}
\quad \Rightarrow \quad
\mathbf{T}_{\text{Drift,x}} =
\begin{bmatrix} 1 & L \\ 0 & 1 \end{bmatrix}
\tag{1}
$$

The same calculations can be made in the yz-plane which means that $\mathbf{T}_{\text{Drift,y}} = \mathbf{T}_{\text{Drift,x}}$.

The transfer matrix in the longitudinal plane acts on the variables $[z, \delta]$. The second variable, δ, is defined as $\delta \equiv \frac{p - p_s}{p_s}$ and since the momentum is constant over a drift space δ is constant, see the second row of equation (3).

The change in z along a drift space can be expressed as $\Delta z = -v\Delta t = -\beta c \Delta t$. The expression for Δt can be achieved from a linear approximation by deriving the expression for $t = \frac{L}{\beta c}$ with respect to s. Note that the last step in this derivation is derived later in this report, see equation (45).

$$
dt = -\frac{L}{c\beta^2} d\beta = -\frac{L}{\beta\gamma^2}\delta
\tag{2}
$$

This expression leads to $dz = \frac{L}{\gamma^2}\delta$. Now we can construct the transfer matrix of a drift space which can be seen in the equation below. Here we transform from the coordinates $[z_i, \delta_i]^T$ at the beginning of the drift space to the coordinates just after, $[z_f, \delta_f]^T$.

$$
\begin{array}{ll}
z_f = & z_i + \dfrac{L}{\gamma^2} \cdot \delta_i \\
\delta_f & = \delta_i
\end{array}
\quad \Rightarrow \quad
\mathbf{T}_{\text{Drift,z}} =
\begin{bmatrix} 1 & \dfrac{L}{\gamma^2} \\ 0 & 1 \end{bmatrix}
\tag{3}
$$

The full 6D transfer matrix of a drift space of length L is achieved by combining the matrices $\mathbf{T}_{\text{Drift,x}}$, $\mathbf{T}_{\text{Drift,y}}$ and $\mathbf{T}_{\text{Drift,z}}$ from equations (1) and (3). The full matrix can be seen below:

$$\mathbf{T}_{\text{Drift}} = \begin{bmatrix} \mathbf{T}_{\text{Drift,x}} & \mathbf{0} & \mathbf{0} \\ \mathbf{0} & \mathbf{T}_{\text{Drift,x}} & \mathbf{0} \\ \mathbf{0} & \mathbf{0} & \mathbf{T}_{\text{Drift,z}} \end{bmatrix} \tag{4}$$

Note that $\mathbf{T}_{\text{Drift,x}} = \mathbf{T}_{\text{Drift,y}}$ and that $\mathbf{0} = \begin{bmatrix} 0 & 0 \\ 0 & 0 \end{bmatrix}$.

2.2.2 Quadrupole

The following derivation is based on [10]. A quadrupole is an element composed of four coils arranged as shown in figure 5. In this figure the transverse field lines can also be seen. The longitudinal field components of quadrupoles is approximated to be zero. The full derivation is based on [10]
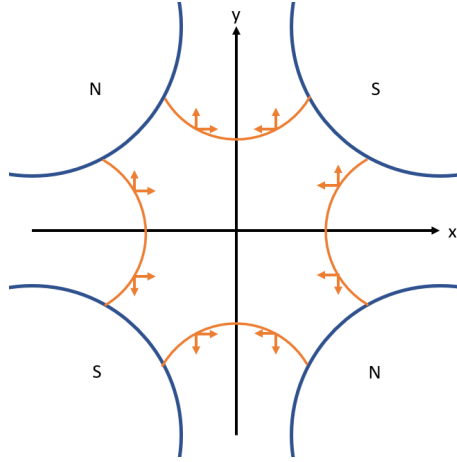

Figure 5: The figure shows placements of the four magnetic poles in a quadrupole. The orange lines are the field lines and the arrows the force components in x and y a particle experiences if it is travelling towards the viewer. There are no field lines in the z-direction excluding edge effects.

The force a charged particle experiences when passing through a quadruple can be described by the Lorentz force:

$$\mathbf{F} = q(\mathbf{E} + \mathbf{v} \times \mathbf{B}) \tag{5}$$

In the quadruple no electrical field is present. In addition, if the field in x-direction is focusing the field in y-direction is defocusing. The field components can therefore be written as:

$$\begin{cases} F_x = & -qv_z B_y = & -qv_z Gx \\ F_y = & qv_z B_x = & qv_z Gy \end{cases} \tag{6}$$

The magnetic field components can be expressed as a linear function of the gradient G as $B_x = Gy$ and $B_y = Gx$ which has been used in equation (6).

To reach the differential equations that describe the motion of a particle in an accelerator a circular orbit can be used. The coordinates (x, y) is the deviation from this orbit, see figure 6.
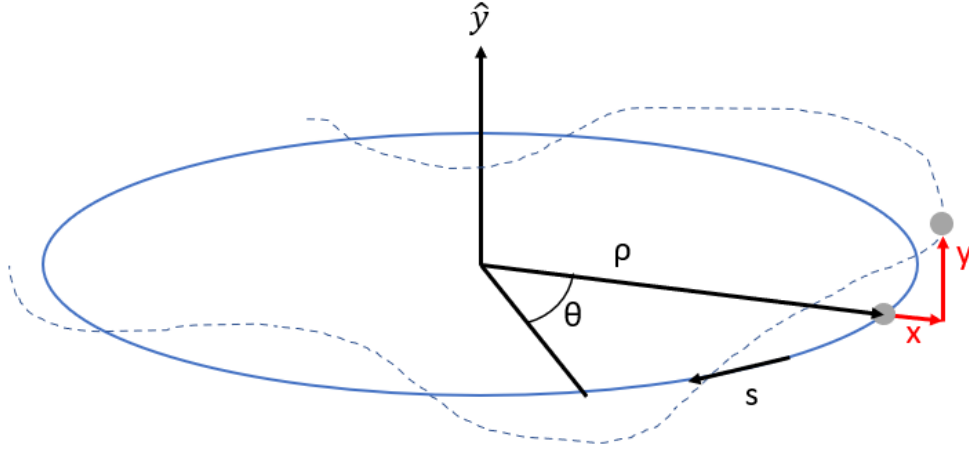
Figure 6: The figure shows how the coordinates x and y are defined. The particle on the circular orbit is the synchronous particle which has the transverse coordinates $(0,0)$ whereas the particle in the dashed line is a particle slightly off from the synchronous particle and therefore has the transverse coordinates (x, y). Also the cylindrical coordinates ρ and θ are included in the figure.

The reference particle is moving in an orbit of turning radius ρ. For this particle $p_x = p_y = 0$ and $x = y = 0$ and $p = p_0$. However, a particle not following the reference orbit has non-zero p_x, p_y, x and y and $p \neq p_0$. However, we assume that the deviations are small so that $x, y << \rho$ and $p_x, p_y << p_0$. Due to this, only the linear terms of $\mathbf{B}$ are taken into account.

The magnetic rigidity, defined in equation (7), refers to that the resistance a beam has to deflection by magnetic fields. The higher momentum a particle has the higher is the magnetic rigidity. [11]

$$B_0 \rho = \frac{P}{q} \tag{7}$$

If the Taylor-expansion of the y-component of the magnetic field is divided by the magnetic rigidity the following is obtained:

$$\frac{B_y(x)}{P/q} = \frac{B_0}{B_0 \rho} + \frac{G_{\text{quad}}}{P/q} x + ... = \frac{1}{\rho} + k_1 + ... \tag{8}$$

Here the dependence $B_y = Gx$ was used for the second term. The parameter k_1 is known as the normalised focusing strength of a quadrupole. The index 1 indicates that this is the strength of a quadrupole. Index 2 would be used for the strength of a sextupole and can be derived from the third term in the Taylor expansion and so on. The $k_0 = \frac{1}{\rho}$ similarly describes the field of a dipole magnet and is called weak focusing.

The acceleration in radial direction can be described using the cylindrical coordinates as: [12]

$$a_r = \frac{d^2 r}{dt^2} - r\left(\frac{d\theta}{dt}\right)^2 \tag{9}$$

The radial coordinate can be expressed as a constant turning radius plus a *small* deviation, $r = \rho + x$, and that $v_s = v_\theta = r\omega = r\frac{d\theta}{dt}$. Using this, the following expression can be reached:

$$a_r = \frac{d^2}{dt^2}(\rho + x) - \frac{v^2}{(\rho + x)} \tag{10}$$

The movement of the particles can be described by the fore equilibrium $F_{\text{centrifugal}} = -F_{\text{lorentz}}$ which leads to equation (11). Note that $F_{\text{centrifugal}} = -ma_r$.

$$m(\frac{d^2}{dt^2}(\rho + x) - \frac{v^2}{\rho + x}) = -qB_y v \tag{11}$$

Since $\rho = const$ the term $\frac{d^2\rho}{dt^2} = 0$. In addition, $\frac{1}{\rho+x} \approx \frac{1}{\rho}(1 - \frac{x}{\rho})$ if x is small. This transforms equation (11) to, if both sides also are divided by m:

$$\frac{d^2 x}{dt^2} - \frac{v^2}{\rho}(1 - \frac{x}{\rho}) = -\frac{qB_y v}{m} = -\frac{qvB_0}{m} - \frac{xqvG_{\text{quad}}}{m} \tag{12}$$

where the linear approximation of B_y is used, see equation (8) without dividing by the magnetic rigidity. Next the independent variable is changed from t, time, to s, the coordinate along the path of the particle.

$$\frac{dx}{dt} = \frac{dx}{ds}\frac{ds}{dt} = x'v$$
$$\frac{d^2 x}{dt^2} = x''v^2 + x'2v\frac{dv}{ds} \approx x''v^2 \tag{13}$$

Put into equation (12) and dividing by v^2 give:

$$x'' - \frac{1}{\rho}(1 - \frac{x}{\rho}) = -\frac{qB_0}{mv} - \frac{xqG_{\text{quad}}}{mv} = -\frac{1}{\rho} - kx \tag{14}$$

Note that $p = mv$, the magnetic rigidity is $P/q = B_0\rho$ and that the normalised focusing strength is given by equation (15) according to equation (8).

$$k_1 = \frac{G_{\text{quad}}}{p/q} \tag{15}$$

Cleaning up equation (14) results in

$$x'' + Kx = 0 \tag{16}$$

where $K = \frac{1}{\rho^2} + k_1$. The same derivation can be made for vertical motion which will result in $y'' + Ky = 0$. But here $K = -k_1$ since $\frac{1}{\rho^2} = 0$ due to no bend in the vertical direction. The sign change of k_1 is due to the opposite signs of B_y and B_x in equation (6). The term $\frac{1}{\rho^2}$ is called weak focusing. In a linear accelerator this term goes to zero as the turning radius $\rho \to \infty$ for a straight path. To summarize:

$$x'' + Kx = 0 \quad \text{where} \quad \begin{cases} K_{\text{hor}} = \frac{1}{\rho^2} + k_1 \\ K_{\text{ver}} = -k_1 \end{cases} \tag{17}$$

When $K > 0$ the ansatz $x(s) = a_1 \cdot \cos(\omega s) + a_2 \cdot \sin(\omega s)$ can be used together with the initial conditions x_0 and x_0' to reach the following solution:

$$\begin{cases} x(s) = x_0 \cdot \cos(\sqrt{K}s) + \frac{x_0'}{\sqrt{K}} \cdot \sin(\sqrt{K}s) \\ x'(s) = -x_0 \cdot \sqrt{K} \cdot \sin(\sqrt{K}s) + x_0' \cdot \cos(\sqrt{K}s) \end{cases} \tag{18}$$

Which results in the following transfer matrix for a focusing quadrupole of length L:

$$\mathbf{T}_{QF} = \begin{bmatrix} \cos(\sqrt{K}L) & \frac{1}{\sqrt{K}}\sin(\sqrt{K}s) \\ -\sqrt{K}\sin(\sqrt{K}L) & \cos(\sqrt{K}L) \end{bmatrix} \tag{19}$$

When $K < 0$ the ansatz $x(s) = a_1 \cdot \cosh(\omega s) + a_2 \cdot \sinh(\omega s)$ results in the following transfer matrix for defocusing quadrupoles of length L:

$$\mathbf{T}_{QD} = \begin{bmatrix} \cosh(\sqrt{|K|}L) & \frac{1}{\sqrt{|K|}}\sinh(\sqrt{|K|}s) \\ \sqrt{|K|}\sinh(\sqrt{|K|}L) & \cosh(\sqrt{|K|}L) \end{bmatrix} \tag{20}$$

Note that when $K = 0$, $\mathbf{T}_{\text{QF}} = \mathbf{T}_{\text{QF}} = \mathbf{T}_{\text{drift}}$. The focal length is then:

$$f = \frac{1}{KL} \tag{21}$$

If the focal length, f is much larger than the length L of a quadrupole, the quadrupole can be approximated to be thin. The matrix for a thin quadrupole is achieved by letting $L \to 0$ while $f = const$ which means that $K \cdot L = const$. Using these limits on $\mathbf{T}_{\text{QF}}$ and $\mathbf{T}_{\text{QD}}$ results in the following transfer matrices:

$$\mathbf{T}_{\text{QF,thin}} = \begin{bmatrix} 1 & 0 \\ -\frac{1}{f} & 1 \end{bmatrix} \qquad \mathbf{T}_{\text{QD,thin}} = \begin{bmatrix} 1 & 0 \\ \frac{1}{f} & 1 \end{bmatrix} \tag{22}$$

Since there are no force components in the z-direction the quadrupole is a drift space in longitudinal direction. This results in the full 6D-matrix for a focusing quadrupole being:

$$\mathbf{T}_{\text{QF}} = \begin{bmatrix} \mathbf{T}_{\text{QF}} & \mathbf{0} & \mathbf{0} \\ \mathbf{0} & \mathbf{T}_{\text{QD}} & \mathbf{0} \\ \mathbf{0} & \mathbf{0} & \mathbf{T}_{\text{Drift,z}} \end{bmatrix} \tag{23}$$

where $\mathbf{0} = \begin{bmatrix} 0 & 0 \\ 0 & 0 \end{bmatrix}$. The transfer matrix for a defocusing quadrupole can be constructed by switching places of $\mathbf{T}_{\text{QF}}$ and $\mathbf{T}_{\text{QD}}$. If the quadrupole is considered thin, the matrices used are then $\mathbf{T}_{\text{QF,thin}}$ and $\mathbf{T}_{\text{QD,thin}}$.

2.2.3 RF cavity

To derive the transfer matrix of an accelerating RF cavity, one can start with the equation of motion for a particle of mass m and charge q moving in an electromagnetic field, see equation (24). The particle will be assumed to travel very close to the z-axis with a direction similar to the z-direction, meaning that paraxial approximations can be made.

$$\frac{d\mathbf{p}}{dt} = q\left(\mathbf{E} + \frac{\mathbf{P}}{\gamma m} \times \mathbf{B}\right) \tag{24}$$

This results in a vector with the Cartesian components

$$\begin{cases} \dot{p}_x = & q\left(E_x + \frac{p_z}{\gamma m}(y' B_z - B_y)\right) \\ \dot{p}_y = & q\left(E_y + \frac{p_z}{\gamma m}(B_x - x' B_z)\right) \\ \dot{p}_z = & q\left(E_z + \frac{p_z}{\gamma m}(x' B_y - y' B_x)\right) \end{cases} \tag{25}$$

where the definitions

$$\frac{dx}{ds} = x' = \frac{p_x}{p_z} \Rightarrow p_x = p_z \cdot x' \quad \text{and} \quad \frac{dy}{ds} = y' = \frac{p_y}{p_z} \Rightarrow p_y = p_z \cdot y' \tag{26}$$

have been used. The magnetic field in this cavity is approximated to be zero, meaning that all B components will be set to zero from now on. In order to construct a transfer matrix, the change of x and x' in relation to the position along its path s needs to be derived. This is achieved by evaluating the expression for $\frac{dx'}{ds}$, seen below

$$\frac{dx'}{ds} = \frac{d(p_x/p_z)}{dt}\frac{dt}{ds} = \frac{1}{\beta_s c} \cdot \frac{\dot{p}_x - \dot{p}_z \cdot x'}{p_z} \tag{27}$$

Note that $\frac{dt}{ds} = \frac{1}{v} = \frac{1}{\beta_s c}$ where $\beta_s \approx \beta_z$ due to the paraxial approximation. If equation (25) is plugged into equation (27) the expression in equation (28) is obtained. Note that $\frac{dy'}{ds}$ was reached by using equation (27) but where p_x was switched to p_y. Also note that $p_z = \gamma \beta_z mc$.

$$\begin{aligned}
\frac{dx'}{ds} &= \frac{q}{\gamma \beta_s^2 mc^2}(E_x - x' \cdot E_z) \\
\frac{dy'}{ds} &= \frac{q}{\gamma \beta_s^2 mc^2}(E_y - y' \cdot E_z)
\end{aligned} \tag{28}$$

These are the equations for the transverse movement. To make these calculations usable, the EM-field is approximated by the following linear approximation:

$$E_x \approx E_{x0} + \frac{\partial E_x}{\partial x} \cdot x + \frac{\partial E_x}{\partial y} \cdot y + \frac{\partial E_x}{\partial z} \cdot z \tag{29}$$

The approximation is similar for the fields in the y and z directions.

In the x-direction the expression for $\frac{dx'}{ds}$ can be rewritten by plugging equation (29) into equation (28). This results in the following:

$$\frac{dx'}{ds} = \frac{q}{\gamma_s \beta_s^2 mc^2}(E_{\text{xo}} - E_{\text{zo}}x' + \frac{\partial E_x}{\partial x}x + \frac{\partial E_x}{\partial y}y + \frac{\partial E_x}{\partial z}z) \tag{30}$$

Then we neglect all terms that are not proportional to x or x'. This is under the assumption that there are no cross terms in the matrix, i.e. that x and x' only depends on x and x' and not on y's or z's.

For the next step some specifics about the field is required. For an accelerating RF cavity the EM field can be described as:

$$\begin{aligned}
E_z(r,s,t) &= E_{z0}(s) \cdot \cos(\omega \cdot t + \varphi) \\
E_x(r,s,t) &= -\frac{1}{2}\frac{dE_{z0}(s)}{ds} \cdot x \cdot \cos(\omega \cdot t + \varphi) = \frac{\partial E_x}{\partial x} \cdot x \\
E_y(r,s,t) &= -\frac{1}{2}\frac{dE_{z0}(s)}{ds} \cdot y \cdot \cos(\omega \cdot t + \varphi) = \frac{\partial E_y}{\partial y} \cdot y
\end{aligned} \tag{31}$$

For only x the equation for $\frac{dx'}{ds}$ becomes the expression in equation (32).

$$\frac{dx'}{ds} = \frac{q}{\gamma_s \beta_s^2 mc^2}(-E_{z0} \cdot \cos(\varphi) \cdot x' + \frac{\partial E_x}{\partial x} \cdot x) \tag{32}$$

Using a linear approximation it can be stated that (note that we approximate $ds \approx dz$)

$$x'_{n+1} - x'_n = \frac{dx'_n}{ds}dz \quad \Rightarrow$$
$$x'_{\text{n}+1} = \frac{q}{\gamma_s \beta_s^2 mc^2}(\frac{\partial E_x}{\partial x}) \cdot dz \cdot x_n + (1 - \frac{q}{\gamma_s \beta_s^2 mc^2}E_{z0} \cdot \cos(\varphi) \cdot dz) \cdot x'_n) = m_{21\text{x}} \cdot x_n + m_{22\text{x}} \cdot x'_n \tag{33}$$

If the expressions for the transverse derivatives of the electric field from equation (31) are inserted into the expressions for the coefficients $m_{21\text{x}}$ and $m_{22\text{x}}$ in equation (33), the resulting equations are:

$$\begin{aligned}
m_{21\text{x}} &= \frac{q}{\gamma_s \beta_s^2 mc^2}(-\frac{1}{2} \cdot dE_{z0}\cos(\varphi) + \frac{\beta\omega}{2c}E_{z0}dz \cdot \sin(\varphi)) \\
m_{22\text{x}} &= 1 - \frac{q}{\gamma_s \beta_s^2 mc^2}E_{z0} \cdot \cos(\varphi) \cdot dz
\end{aligned} \tag{34}$$

Next, $x_{\text{n}+1}$ was also linearly approximated:

$$x_{\text{n}+1} = x_n + \frac{x_n}{ds}dz = x_n + x'_n \cdot dz \tag{35}$$

which means the the matrix $\mathbf{T}_{\text{xx}}$ is given by

$$\mathbf{T}_{\text{xx}} = \begin{bmatrix} 1 & 0 \\ m_{21\text{x}} & m_{22\text{x}} \end{bmatrix} \tag{36}$$

10

Due to assumed the cylindrical symmetry $\mathbf{T}_{xx} = \mathbf{T}_{yy}$.

The longitudinal motion can be described by the two parameters $z = -\frac{\varphi}{2\pi} \cdot \beta\lambda$ and $\delta = \frac{p - p_s}{p_s} = \frac{\Delta p}{p_s} = \frac{dp}{p}$ where p_s is the momentum of a particle in perfect sync with the RF accelerating cavity.

To express the equations of motion in terms of z and δ, the expression for $\frac{dp}{ds}$ was first derived using $p^2 = p_x^2 + p_y^2 + p_z^2 = p_z^2(1 + x'^2 + y'^2)$:

$$\frac{dp}{ds} = \frac{\frac{dp_z}{ds} \cdot (1 + x'^2 + y'^2) + p_z \cdot (x' \cdot \frac{dx'}{ds} + y' \cdot \frac{dy'}{ds})}{\sqrt{1 + x'^2 + y'^2}} \tag{37}$$

If the known expressions for $\frac{dx'}{ds}$, $\frac{dy'}{ds}$, $\dot{p}_z$ and $\frac{dp_z}{ds} = \frac{dp_z}{dt} \cdot \frac{dt}{ds} = \frac{\dot{p}_z}{\beta_z c}$ are plugged into (37) the expression in equation (38) is obtained. Here all quadratic terms of x' and y' have been removed due to the paraxial approximation.

$$\frac{dp}{ds} = \frac{q}{\beta_z c}(E_z + x' \cdot E_x + y' \cdot E_y) \tag{38}$$

However, the expression for $\frac{d\delta}{ds}$ is needed to form the matrix that transforms the parameters z and δ in a cavity. The relation between $\frac{d\delta}{ds}$ and $\frac{dp}{ds}$ is

$$\frac{d\delta}{ds} = \frac{d}{ds}\frac{p - p_s}{p_s} = \frac{1}{p_s} \cdot (\frac{dp}{ds} - (1 + \delta) \cdot \frac{dp_s}{ds}) \tag{39}$$

A particle travelling with the momentum p_s is a synchronous particle whereas a particle with momentum p is an arbitrary particle. The major difference between the two particles is the speed, i.e. β because the phase of the two particles are approximately the same, $\varphi \approx \varphi_s$. The relations between β and β_s is $\beta = \beta_s + d\beta$. In order to write this equation as a linear function of z and δ the following equality is useful:

$$\frac{dp}{ds} - \frac{dp_s}{ds} = \frac{q}{\beta c}(E_{z0} + \frac{\partial E_z}{\partial z}z) - \frac{q}{\beta_s c}E_{z0}) \tag{40}$$

Here the following relations were used:

$$\frac{dp}{ds} = \frac{q}{\beta c}E_z = \frac{q}{\beta c}(E_{z0} + \frac{\partial E_z}{\partial z}z)$$
$$\frac{dp_s}{ds} = \frac{q}{\beta_s c}E_{z0} \tag{41}$$

Simplifying equation (40) further by using $\frac{1}{\beta} - \frac{1}{\beta_s} = \frac{-d\beta}{\beta_s(\beta_s + d\beta)} \approx -\frac{d\beta}{\beta_s^2}$ gives

$$\frac{dp}{ds} - \frac{dp_s}{ds} \approx \frac{q}{c}E_{z0}(\frac{-d\beta}{\beta_s^2}) + \frac{q}{\beta_s c}\frac{\partial E_z}{\partial z}z \tag{42}$$

In order to get the right hand side to be a function of constants and δ and z, $d\beta$ has to be rewritten as a function of δ. This can be done using the following approximation:

$$d\beta = \beta - \beta_s = \frac{\gamma(\beta - \beta_s)}{\gamma} \approx \frac{\gamma\beta - \gamma\beta_s}{\gamma_s} \tag{43}$$

Note that the approximation of the denominator being approximately γ_s could be made due to the numerator being $\gamma d\beta$ which means that we can neglect all second order terms. Next, $\gamma\beta_s$ is evaluated by neglecting all $d\beta^2$ terms and using $\frac{1}{\sqrt{(1-x)}} \approx 1 + \frac{x}{2}$.

$$\gamma\beta_s = \frac{\beta_s}{\sqrt{1 - (\beta_s + d\beta)}} \approx \frac{\gamma_s\beta_s}{\sqrt{1 - 2\beta_s\gamma_s^2 d\beta}} \approx \gamma_s\beta_s(1 + \gamma_s^2\beta_s d\beta) \tag{44}$$

Plugging (44) into equation (43) and using $1 + \gamma_s^2\beta_s^2 = \gamma_s^2$ gives

11

$$d\beta = \frac{\gamma\beta - \gamma_s\beta_s}{\gamma_s^3} = \frac{mc\beta_s}{mc\beta_s}\frac{\gamma\beta - \gamma_s\beta_s}{\gamma_s^3} = \frac{\beta_s}{\gamma_s^2}\delta \tag{45}$$

Plugging this expression for $d\beta$ into equation (42) gives the expression in equation (46), where the last step can be done due to $\frac{1}{\gamma_s^2} = (1 - \beta^2)$.

$$\frac{dp}{ds} - \frac{dp_s}{ds} \approx \frac{-q}{\beta_s\gamma_s^2 c}E_{z0}\delta + \frac{q}{\beta_s c}\frac{\partial E_z}{\partial z}z = \frac{-q}{\beta_s c}E_{z0}(1 - \beta_s^2)\delta + \frac{q}{\beta_s c}\frac{\partial E_z}{\partial z}z \tag{46}$$

Going back to the expression for $\frac{d\delta}{ds}$, equation (39), the following expression is obtained by plugging in the equation (46)

$$\frac{d\delta}{ds} = \frac{1}{p_s} \cdot \left(\frac{dp}{ds} - \frac{dp_s}{ds} - \frac{dp_s}{ds} \cdot \delta\right) \approx \frac{q}{\gamma_s\beta_s^2 mc^2}\left(-E_{z0}(2 - \beta_s^2) \cdot \delta + \frac{\partial E_z}{\partial z} \cdot z\right) \tag{47}$$

To construct the transfer matrix in the longitudinal direction explicit Euler time integration is used once again, meaning

$$\delta_{n+1} = \frac{d\delta_n}{ds}dz + \delta_n = \frac{q}{\gamma_s\beta_s^2 mc^2}\frac{\partial E_z}{\partial z} \cdot dz \cdot z_n + (1 - (2 - \beta_s^2) \cdot E_{z0}) \cdot dz \cdot \delta_n = m_{21z} \cdot z_n + m_{22z} \cdot \delta_n \tag{48}$$

Using the EM-fields of a cavity, equation (31), the coefficients m_{21z} and m_{22z} becomes

$$
\begin{aligned}
m_{21z} &= \frac{q}{\gamma_s\beta_s^2 mc^2}dE_{z0} \cdot \cos(\varphi) \\
m_{22z} &= 1 - \frac{q}{\gamma_s\beta_s^2 mc^2} \cdot (2 - \beta_s^2) \cdot E_{z0} \cdot \cos(\varphi) \cdot dz
\end{aligned} \tag{49}
$$

This means that the matrix $\mathbf{T}_{zz}$ is given by:

$$\mathbf{T}_{zz} = \begin{bmatrix} 1 & 0 \\ m_{21z} & m_{22z} \end{bmatrix} \tag{50}$$

The [6x6] transfer matrix of one point in a RF cavity reads:

$$\mathbf{T}_{gap} = \begin{bmatrix} \mathbf{T}_{xx} & \mathbf{0} & \mathbf{0} \\ \mathbf{0} & \mathbf{T}_{yy} & \mathbf{0} \\ \mathbf{0} & \mathbf{0} & \mathbf{T}_{zz} \end{bmatrix} \tag{51}$$

since it is assumed that the crossterms between x, y and z can be neglected. Here $\mathbf{0}$ is a [2x2] zero matrix, $\mathbf{T}_{xx}$ and $\mathbf{T}_{yy}$ are given by equation (36) and $\mathbf{T}_{zz}$ is given by (50). To get the transfer matrix of an entire cavity, the cavity can be thought of as thin gaps with drift spaces in between, see figure 7. The thin gaps are assumed to have a constant electromagnetic field and the field in each of these points are given by a field map. The field maps used in this degree project have 500 points.

Figure 7: The figure shows how one RF cavity can be approximated by a finite number of thin gaps with drift spaces in between.

The transfer matrix of an entire cavity is then given by the combination of these components, which can be seen in equation (52).

$$\mathbf{T}_{RF} = \mathbf{T}_{gap}(z_n) \cdot \mathbf{T}_{dift} \cdot \mathbf{T}_{gap}(z_{n-1}) \cdot \mathbf{T}_{dift} \cdot \ldots \cdot \mathbf{T}_{dift} \cdot \mathbf{T}_{gap,1}(z_1) \tag{52}$$

where $\mathbf{T}_{gap}$ is given by the matrix of a drift space of length dz, see equation (4).

$$\mathbf{T}_{\text{gap}} = \begin{bmatrix} 1 & dz & 0 & 0 & 0 & 0 \\ 0 & 1 & 0 & 0 & 0 & 0 \\ 0 & 0 & 1 & dz & 0 & 0 \\ 0 & 0 & 0 & 1 & 0 & 0 \\ 0 & 0 & 0 & 0 & 1 & \dfrac{dz}{\gamma_s^2} \\ 0 & 0 & 0 & 0 & 0 & 1 \end{bmatrix} \tag{53}$$

The matrix $\mathbf{T}_{\text{gap}}(z_i)$ is given by extracting the values of $E_{z0}(z_i)$ and $dE_Z(z_i)$ from a field map of the RF cavity. This entire derivation is based on the TraceWin documentation [8].

2.3 Twiss Parameters

As stated in section 2.2, Twiss parameters are a convenient way to describe the particle trajectories in an accelerator. The parameters are β, α, γ and the phase function ψ. The following derivation is inspired by [10].

Twiss parameters are connected to the trajectory through the equation of motion:

$$u'' + k(z)u = 0 \tag{54}$$

which can be solved using the following ansatz:

$$u(z) = \sqrt{\epsilon}\sqrt{\beta(z)}\cos[\psi(z) - \psi_0] \tag{55}$$

where ϵ and ψ_0 are integration constants. Plugging this ansatz into equation (54) yields the following two conditions:

$$\frac{1}{2}(\beta\beta'' - \frac{1}{2}\beta'^2) - \beta^2\psi'^2 + \beta^2 k = 0 \tag{56}$$

$$\beta'\psi' + \beta'' = 0 \tag{57}$$

The chosen normalisation for the solution is:

$$\beta\psi' = const. = 1 \tag{58}$$

Equation (57) together with equation (58) gives the following expression for the phase function as a function of the beta function:

$$\psi(z) = \int_0^z \frac{dz'}{\beta(z')} + \psi_0 \tag{59}$$

The β-function itself is achieved by using equations (56) and (58). Firstly, the expression below is reached:

$$\frac{1}{2}\beta\beta'' - \frac{1}{4}\beta'^2 + \beta^2 k = 1 \tag{60}$$

this together with the definitions:

$$\alpha = -\frac{1}{2}\beta' \quad \& \quad \gamma = \frac{1 + \alpha^2}{\beta} \tag{61}$$

gives the following equation for β:

$$\beta'' + 2k\beta - 2\gamma = 0 \tag{62}$$

The solution to (62), i.e. $\beta(z)$ together with the phase function $\psi(z)$ can be used to build a real valued solution for the equation of motion, equation (54). This gives the Courant-Snyder invariant:

13

$$\gamma u^2 + 2\alpha u u' + \beta u'^2 = \epsilon \tag{63}$$

This is also an equation of an ellipse with the area $\pi\epsilon$ in the phase-space of the particle, where ϵ is the emittance. Note that the emittance is invariant.

The transformation of the Twiss parameters in one position s_0 to another position s_1 can be calculated using the transfer matrix of the lattice elements between the two points. This is described in the next section. The Twiss parameters can also be connected to the σ-matrix of a beam. The sigma matrix contains statistical information about the beam and the uncoupled version can be seen below: [10]

$$\boldsymbol{\sigma}_x = \begin{bmatrix} < x'^2 > & < -xx' > \\ < -x'x > & < x^2 > \end{bmatrix} = \epsilon \begin{bmatrix} \beta_x & -\alpha_x \\ -\alpha_x & \gamma_x \end{bmatrix} \tag{64}$$

From this the dependence equation 65 is reached which can be connected to the phase ellipse in figure 2. The area of the ellipse is $Area = \pi[\det(\boldsymbol{\sigma}_x)]^{1/2} = \pi\epsilon_x$. [9]

$$\sigma_x = \sqrt{\epsilon\beta} \quad \& \quad \sigma_{x'} = \sqrt{\frac{\epsilon}{\beta}} \tag{65}$$

The matrices σ_y and σ_z are similarly defined if no coupling is present, i.e that xx', yy' and $z\delta$ does not depend on each other. The full 6D matrix is therefore:

$$\boldsymbol{\sigma}_{UC} = \begin{bmatrix} \boldsymbol{\sigma}_x & \mathbf{0} & \mathbf{0} \\ \mathbf{0} & \boldsymbol{\sigma}_y & \mathbf{0} \\ \mathbf{0} & \mathbf{0} & \boldsymbol{\sigma}_z \end{bmatrix} \tag{66}$$

2.4 Phase Advance

The Phase advance is how much the particle rotates in the phase space between two points, s_1 and s_2, in a lattice. Usually the phase advance in each FODO cell of a lattice is calculated, meaning halfway through a focusing quad until halfway through the next focusing quad. TraceWin calculates the phase advance in two different ways to calculate both the structural phase advance and the beam phase advance.

2.4.1 Structural Phase advance

The structural phase advance is calculated from the transfer matrix. The 2D transfer matrix of each dimension can be rewritten with the Twiss parameters and the phase advance as in equation (67). [6]

$$\mathbf{T}_{s_1 \rightarrow s_2} = \begin{bmatrix} (\frac{\beta_2}{\beta_1})^{1/2}(\cos\Delta\mu + \alpha_1\sin\Delta\mu)) & (\beta_1\beta_2)^{1/2}\sin\Delta\mu \\ -(\beta_1\beta_2)^{-1/2}[(1+\alpha_1\alpha_2)\sin\Delta\mu + (\alpha_2\alpha_1)\cos\Delta\mu] & (\frac{\beta_1}{\beta_2})^{1/2}(\cos\Delta\mu - \alpha_2\sin\Delta\mu) \end{bmatrix} \tag{67}$$

This matrix is the transfer matrix from point s_1 to point s_2. When the Twiss parameters are the same in these two points, the matrix in (67) becomes (68).

$$\mathbf{T}_{s_1 \rightarrow s_2} = \begin{bmatrix} (\cos\Delta\mu + \alpha\sin\Delta\mu)) & \beta\sin\Delta\mu \\ -\gamma\sin\Delta\mu & (\cos\Delta\mu - \alpha\sin\Delta\mu) \end{bmatrix} \tag{68}$$

From this the phase advance can be calculated as

$$\Delta\mu_x = \arccos(\frac{Tr(\mathbf{T}_{xx})}{2}) ; \quad \text{where} \quad \mathbf{T} = \begin{bmatrix} \mathbf{T}_{xx} & \mathbf{T}_{xy} & \mathbf{T}_{xz} \\ \mathbf{T}_{yx} & \mathbf{T}_{yy} & \mathbf{T}_{yz} \\ \mathbf{T}_{zx} & \mathbf{T}_{zy} & \mathbf{T}_{zz} \end{bmatrix} \tag{69}$$

Here $\mathbf{T}$ is the full 6D transfer matrix from s_1 to s_2. In TraceWins documentation, a term related to the coupling of the transverse planes is also present in this expression but all off diagonal 2D matrices are are

zero in these simulations. [8]

If the phase advance of a non-matched section is to be calculated, the matrix in equation (67) can still be used but information about the Twiss parameters before and after is needed. The 2D transfer matrix between points s_1 and s_2 is:

$$\mathbf{T}_{\mathrm{xx}} = \begin{bmatrix} t_{22} & -t_{21} \\ -t_{21} & t_{11} \end{bmatrix} \tag{70}$$

However, when the particle gains energy while passing through the element described by the transfer matrix $\mathbf{T}_{\mathrm{xx}}$ the transverse transfer matrices are multiplied with the factor: [13]

$$k_{\text{energy gain}} = \sqrt{\frac{\beta_o \gamma_o}{\beta_i \gamma_i}} \tag{71}$$

The Twiss paramenets are transformed via the matrix below, where t_{11}, t_{12}, t_{21} and t_{22} are the elements from (70). [6]

$$\begin{bmatrix} \beta_x \\ \alpha_x \\ \gamma_x \end{bmatrix}_2 = \begin{bmatrix} t_{11}^2 & -2t_{11}t_{12} & t_{12}^2 \\ -t_{11}t21 & [t_{11}t_{22} + t_{12}t_{21}] & -t_{12}t_{22} \\ t_{21}^2 & -2t_{21}t_{22} & t_{22}^2 \end{bmatrix} \begin{bmatrix} \beta_x \\ \alpha_x \\ \gamma_x \end{bmatrix}_1 \tag{72}$$

With the help of this, Twiss parameters of every point in the accelerator lattice can be calculated. Going back to equation (67), the phase advance for a non-matched lattice section can therefor be calculated by using t_{12}, β_1 and β_2, see the following:

$$\Delta\mu = \arcsin\left(\frac{t_{12}}{(\beta_1\beta_2)^{1/2}}\right) \tag{73}$$

However, in transverse phase space, this is only true if the particle does *not* gain any energy in the transition between point s_1 and s_2. If the particle gains energy the phase advance will instead be:

$$\Delta\mu = \arcsin\left(\sqrt{\frac{(\beta\gamma)_{\mathrm{rel},2}}{(\beta\gamma)_{\mathrm{rel},1}}} \frac{1}{(\beta_1\beta_2)} t_{12}\right) \tag{74}$$

2.4.2 Beam Phase Advance

An alternative way of calculating the phase advance, is to calculate the beam phase advance using only the parameter β. The phase advance in this case is defined as: [14]

$$\Delta\mu = \int_{s_1}^{s_2} \frac{1}{\beta(s)} ds \tag{75}$$

In order to get an accurate calculation, more than one β value is needed per element.

2.5 Space Charge

The beam current will be high in the ESS linac, 62.5 mA. This means that the beam will experience strong space charge effects. [1]

The equation of motion used in the derivation of the transfer matrices is for single particle movement. When multiple particles move together in a beam the particles affect each others trajectory, this is called collective effects. One of the major collective effects can be described as a space charge distribution that a single particle moves through, the space charge effect. This is usually treated as a perturbation to the single particle motion. The electrical and magnetic field inside a cylindrical space charge distribution of radius a are given by:

15

$$E = \frac{eN}{2\pi\epsilon_0 a^2} r \quad \& \quad B = \frac{eN\nu}{2\pi\epsilon_0 a^2 c^2} r \tag{76}$$

where e is the elementary charge, N is the number of particles per unit length, ϵ_0 is the permittivity in vacuum, r is the particles distance from the center of the cylindrical beam and ν is the the speed of the particles. The resulting force is given by:

$$\mathbf{F} = \frac{e^2 N}{2\pi\epsilon_0 a^2 \gamma^2} r\hat{r} \tag{77}$$

The linear dependence on r is similar to the force of a defocusing lens. This is a simple model of space charge, however it does have a defocusing effect. Therefore, one way to counter the effects of space charge is to overfocus a lattice. In addition to the defocsuing effect, space charge also lead to tune shift and coherent instability. [15]

3 Retuning procedure

3.1 Lattice file

An accelerator can be described by a Lattice file. This is a file containing information about each element in an accelerator. In this thesis, lattice files adapted to the simulation program TraceWin were used. Here each element had a row of information in a `.dat` file. The elements used for the retuning routine are drift spaces, quadrupoles and cavities.

The variable needed to build a transfer matrix of a drift space is the length, which is then plugged into equations (1) and (3). Similarly, the transfer matrix for a specific quadrupole is created using the length and the gradient defined for that quadrupole in the lattice file.

To create the transfer matrix of an RF cavity, the length, amplitude and phase are needed. The field maps for each type of cavity is saved in separate files. The length and φ_{in} are plugged into equations (34) and (49). The E_z in these formulas are the field map values in this point of the cavity multiplied with *amp*. The *amp* value is the percentage of full power the cavity is set to.

Examples of lattice file structures can be seen in section 3.5.1.

3.2 Short description of solution method

The process of retuning is done in python and is boiled down to these six steps:

1. Define failed cavity as type (SPK,MBL or HBL) and number cavity of that type. (User input)

2. Define lattice section of lattice containing the four closest cavities to the offline one.

3. Vary the settings of the four closest cavities using a genetic algorithm by comparing the transfer matrix of the defined lattice section for the fully functioning accelerator and the offline and retuned case. Choose the settings where the longitudinal transfer matrix is closest to the nominal case.

4. Change the downstream phase of all elements by calculating the optimal input phase for each of the downstream cavities.

5. Vary the settings of the four closest quadrupoles and compare the transverse transfer matrix of this section to the nominal transfer matrix of the same section and choose the closest solution. Note that calculated cavity settings from the longitudinal matching, step 3, are used when calculation the transfer matrix of this lattice section.

6. Update the settings of the quadrupoles and cavities in the nominal lattice file.

3.3 Genetic Algorithm

The solutions calculated in steps 3 and 5 are reached by using a genetic algorithm (GA). A genetic algorithm is a solution method that can be described by the following scheme: [16]
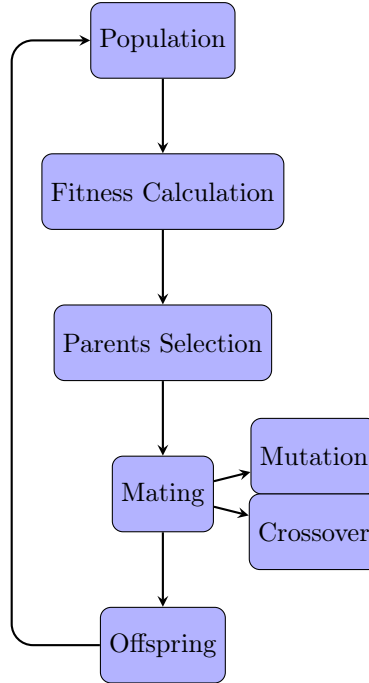
Figure 8: The figure shows the steps of a genetic algorithm.

First a random set of N solutions are generated, this is a *Population*. A solution is a set of n_{vars} variables and each variable can be limited to a set interval. In order to determine how good a solution is, it is given a value based on a fitness function. The fitness function is defined by the problem to be solved and calculates a value using the n_{vars} variables, this is the *Fitness Calculation*. In the genetic algorithm used in this report the fitness value is in between $-\infty$ and 0 and the closer to zero the fitness value is the better the solution. The fitness function used will be described later in this section.

When the fitness value of all solutions in a populations is calculated the worst solutions are switched out for the solution that gives the best fitness value. The genetic algorithm used in the code switches out the worst fifth of the set of solutions. This is the *Parents Selection*. The best solution of the entire set is saved outside the loop.

The parents are then used to create an offspring by mutation and crossover. The mutation is done by multiplying some of the variables in a population by a randomized factor. As an example this random factor can be $(1 \pm x(1 - \frac{t}{\max\_\text{Gen}}))$ where x is a random number in the interval $[0, 1]$, t is what generation the current population is and $\max\_\text{Gen}$ is the maximum number of generations that will be calculated. This results in smaller changes the more generations that have already been calculated. In addition, the sign is randomized with equal probability. The number of variables mutated is determined by the degree of mutation which in turn is a number in the interval $[0, 1]$. If it is 1, every variable in all solutions are mutated.

Moreover, the solutions are after the mutations crossed over. Some variables are switched around between solutions, however variable 1 is only switched with another variable 1 etc. The number of variables being swapped is determined by the degree of crossover. Similar to the degree of mutation, the degree of crossover is a number in the interval $[0, 1]$. The new population after the mutation and crossover is the *Offspring*, i.e. the next generation. If this set of solutions has a solution with a better fitness value than the previous one, the new best solution is saved. Otherwise the previous generations best solution is kept as best solution over all.

The creation of new generations is either stopped when the max number of generations is reached,

max_Gen = 100 is used in this report, or when a fitness limit is reached. A fitness limit is a value of the fitness function that is considered good enough at which point the creating of new generations cease and the latest solution is chosen as the best solution. An alternative point to stop the creation of new generations is when the fitness value changes very little for the last few generations. However, this was not used in the genetic algorithm written for this degree project.

In order to do a retuning of an accelerator lattice, two optimisations are conducted using a genetic algorithm. First a longitudinal matching is done by varying the input phase and the amplitude of the four closest cavities to the offline cavity. This generates 8 variables per solution. Each solution in the population is given a fitness value based on two characteristics, the transfer matrix and the beam phase advance. The cavity settings defined by one possible solution is used to generate a transfer matrix, $\mathbf{T}_{\text{new}}$, of the lattice section containing these four cavities as well as the offline cavity. The longitudinal part of this transfer matrix is compared to the longitudinal part of the transfer matrix, $\mathbf{T}_{\text{ref}}$, generated from the same lattice section but where all cavities are functioning. The fitness value is determined as $-abs(max(\mathbf{T}_{\text{new,zz}} - \mathbf{T}_{\text{ref,zz}}))$ the negative value of the biggest difference between these two [2x2] matrices is the fitness value of the solution. The fitness function is described in the following scheme:
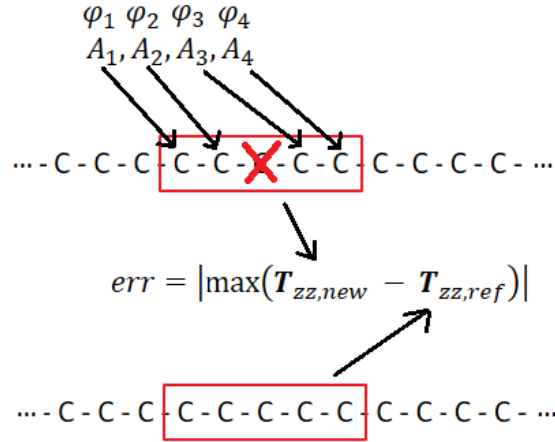
Figure 9: The figure shows how the longitudinal fitness function is defined. The accelerator is here represented as a sequence of cavities "-C-". The chosen lattice section is marked with the red rectangle. The top lattice in the figure is the lattice with the failed cavity, marked with a crossed over C. The four surrounding cavities are given the new cavity settings "$A_1, A_2, A_3, A_4, \phi_1.\phi_2, \phi_3, \phi_4$". This gives a longitudinal transfer matrix named: $\mathbf{T}_{\text{zz,new}}$. The same lattice section of a fully functioning accelerator, i.e. the nominal lattice, is represented as the red rectangle around the five noncrossed "-C-", this section give the reference longitudinal transfer matrix $\mathbf{T}_{\text{zz,ref}}$. The absolute value of the maximum difference of the matrix elements is given by "err".

The value the fitness function generated is then added to a value that determines how good the phase advance is. The longitudinal beam phase advance for the lattice with the settings defined by a solution x is calculated. A linear regression is made in the calculated phase advance. If the slope of the line is not negative, the solutions is appointed the worst possible fitness value, the biggest negative vale of doubles in python. If the slope is negative, the fitness value is determined by the mean value of the residuals. Figure 10 shows how the residuals are calculated. The closer to a smooth line the phase advance is, the better fitness value the solution x is appointed. This fitness value, evaluated from the phase advance quality, is normalized to be the same order of magnitude as the fitness value acquired from the transfer matrix comparison.
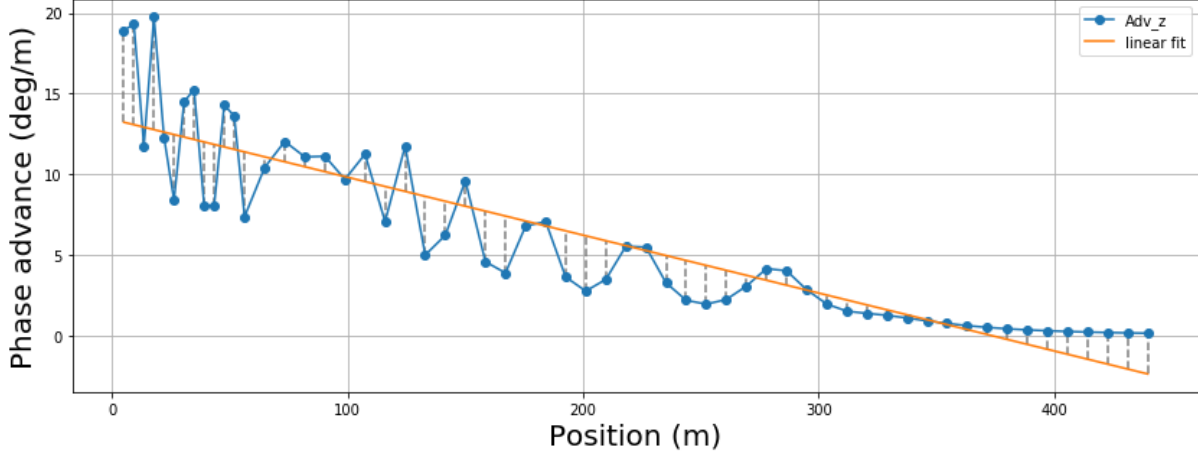
Figure 10: The blue curve is the beam phase advance plotted for an accelerator lattice. The orange curve is then the linear regression to the blue curve. The residuals are drawn as dotted lines.

The phases of all downstream cavities of the previously selected lattice section needs to be updated after the longitudinal retuning routine has been completed. Afterwards a transverse matching is conducted, now with respect to the transverse transfer matrix and the transverse beam phase advance. The matrices are compared using the lattice section containing the four closest quadrupoles. The variables are now the field strengths of these four quadrupoles. These settings are used in the lattice section to generate a transfer matrix, $\mathbf{T}_{\text{new}}$. The transverse part of this transfer matrix is then compared to the transverse part of the nominal transfer matrix of the same section, $\mathbf{T}_{\text{ref}}$. The fitness value is again determined to be $-abs(max(\mathbf{T}_{\text{new,xxyy}} - \mathbf{T}_{\text{ref,xxyy}}))$. The fitness value from the transverse phase advance is obtained by plotting the phase advance in xx' and yy' and then doing a linear regression where the residuals are calculated.

In this degree project the retuning was conducted using only transfer matrix optimization or transfer matrix optimisation together with beam phase advance optimization. A summary of the parameters used in the genetic algorithm used can be seen in table 1. These parameters were set by the original matlab code [17].

Table 1: The table is a summary of all parameters used in the GA for longitudinal matching and the GA for transverse matching. These parameters were used in the original MATLAB code [17].

	longitudinal matching	transverse matching
# variables in solution	8	4
Population size	50	200
maximum number of generations	100	
rate of mutation	15 %	
rate of crossover	50 %	

The evolution of the best fitness value for the longitudinal and transverse matching can be seen in figure 11. Even though the transverse retuning has a population size four times larger than the longitudinal matching, it is still converging slower. The population size can be made even bigger, but to the cost of a longer runtime for the retuning. A populations size of 200 was chosen as a compromise.

20
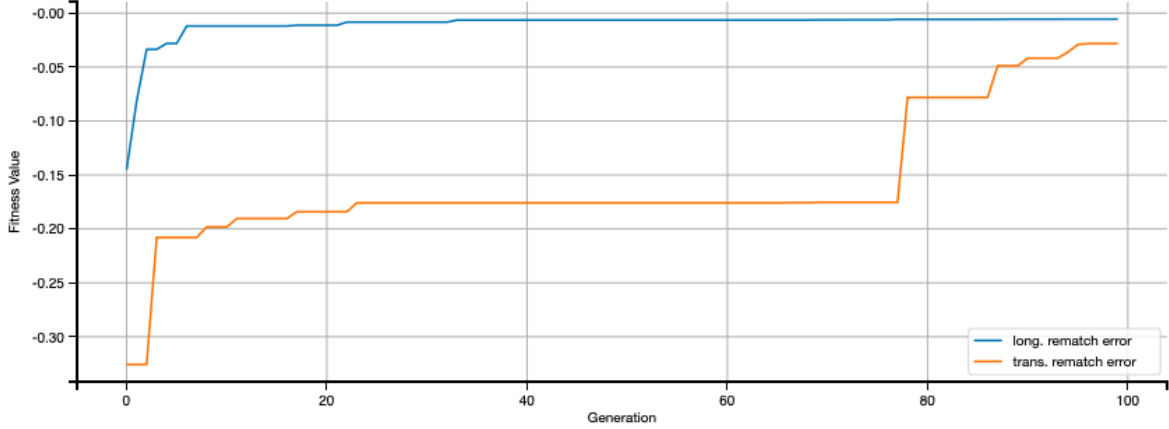
Figure 11: The figures shows the evolution if the fitness value for the longitudinal retuning and the transverse retuning. The fitness function used here only includes transfer matrix optimisation, i.e. the fitness function described in figure 9.

3.4 Time analysis of code

One of the main goals of this degree project was to make a fast rematching. The result of a python profiling of the matching routine using only transfer matrix optimisation was conducted and the result can be seen in table 2. In this run the offline cavity is the 15th spoke cavity.

Table 2: The table shows the result of a time analysis of my rematching code. Only the first 20 rows are included in the table.

ncalls	cumtime	percall	filename:lineno(function)
480/1	1506.572	1506.572	{built-in method builtins.exec}
1	1506.572	1506.572	Sofia_offlineCavity.py:7(<module>)
2	1456.323	728.162	Sofia_GA.py:202(Sofia_myga)
180	1456.166	8.090	Sofia_GA.py:16(cal_pop_fitness)
24002	1454.268	0.061	rematch_functions.py:573(Lattice_2_Matrix)
76287	1438.120	0.019	rematch_functions.py:137(Cavity_Matrix_Input_Phase)
20000	1138.012	0.057	Sofia_offlineCavity.py:107(fitness_q)
20000	1137.916	0.057	rematch_functions.py:1246(Error_t)
75494438	405.599	0.000	<__array_function__ internals>:2(dot)
77865054/77865050	358.447	0.000	{built-in method numpy.core._multiarray_umath.implement_array_function}
4000	317.915	0.079	Sofia_offlineCavity.py:84(fitness)
4000	317.896	0.079	rematch_functions.py:720(Error_z)
1	44.258	44.258	rematch_functions.py:770(Ref_RePhase)
387	22.570	0.058	rematch_functions.py:1063(Phase_Scan)
258	17.518	0.068	rematch_functions.py:994(Phase_Scan_Peak)
408033	12.571	0.000	rematch_functions.py:630(Drift_Matrix)
2321317	11.842	0.000	<__array_function__ internals>:2(concatenate)
75494438	9.430	0.000	multiarray.py:707(dot)
96008	4.964	0.000	rematch_functions.py:670(Quad_Matrix)
1	4.478	4.478	rematch_functions.py:305(Ref_Phase)

The function that takes the most cumulative time is as expected `Sofia_myga`. The reason that this function takes time is that it calculates the fitness value of each solution. This is done using the functions

21

`Error_t` or `Error_z`. These two functions are called many times which results an a high cumulative time despite each individual run being quite fast. Note that the cumulative time of these two functions add up to the cumulative time of the function `cal_pop_fitness`. Most calls of the function `Lattice_2_Matrix` are from either `Error_t` or `Error_z` (all except 2) and these calls make up for the majority of the runtime of these functions. The function `Lattice_2_matrix`, that calculates the 6D transfer matrix, also has a significant runtime. Of the functions `Lattice_2_matrix` calls, the function `Cavity_Matrix_Input_Phase`, that calculates the transfer matrix of a cavity, takes the longest. Each run of this takes about 0.02 seconds and here there is room for improvement. This conclusion is expected as it is known that simulations using field maps are slow.

Another function that is time consuming is the `Ref_RePhase` function that calculates the ultimate phase for all downstream cavities. This function scans possible input phases for the cavities downstream of the offline cavity. The functions that take the most time here is `Phase_Scan` and `Phase_Scan_Peak`. A possible improvement is to narrow the bandwidth of the scan by using the phase adjustment of the first cavity as an educated guess. So instead of scanning between $\pm 180°$, one can possibly scan between $\theta_i \pm 5°$ where θ_i is the input phase of the first cavity downstream from the rematched section of the accelerator.

3.5 Accuracy of nominal simulation

3.5.1 Matrix comparison with TraceWin

In order to know how accurate my simulation of an the accelerator is, I compared the transfer matrix of a simple lattice containing four spoke cavities and four drifts spaces. The TraceWin lattice file is:

DRIFT 141 28 0 0 0
FIELD_MAP 100 988 -1.10293 28 0 0.974792 0 0 Spoke_W_coupler
DRIFT 141 28 0 0 0
FIELD_MAP 100 988 16.4006 28 0 0.886384 0 0 Spoke_W_coupler
DRIFT 141 28 0 0 0
FIELD_MAP 100 988 35.0838 28 0 0.886384 0 0 Spoke_W_coupler
DRIFT 141 28 0 0 0
FIELD_MAP 100 988 43.2861 28 0 0.886384 0 0 Spoke_W_coupler
END

In a lattice file to TraceWin the parameters for a Field map are "FIELD_MAP geom L Input_Phase R k_b k_e K_i K_k FileName". The corresponding configuration for a drift space is "Drift L R R_y R_{x_shift} R_{y_shift}".

The transfer matrix this lattice generated in TraceWin was used as reference and the matrix my program generated was therefore compared to this TraceWin matrix by taking the maximum value of the difference of the matrix element in the xx', yy' and the longitudinal part of the transfer matrices. When calculating the transfer matrix of a cavity a field map is used. The more points in the field map the more accurate the matrix calculations is, see figure 12. However, the more points in the field map used, the more costly is the calculation.
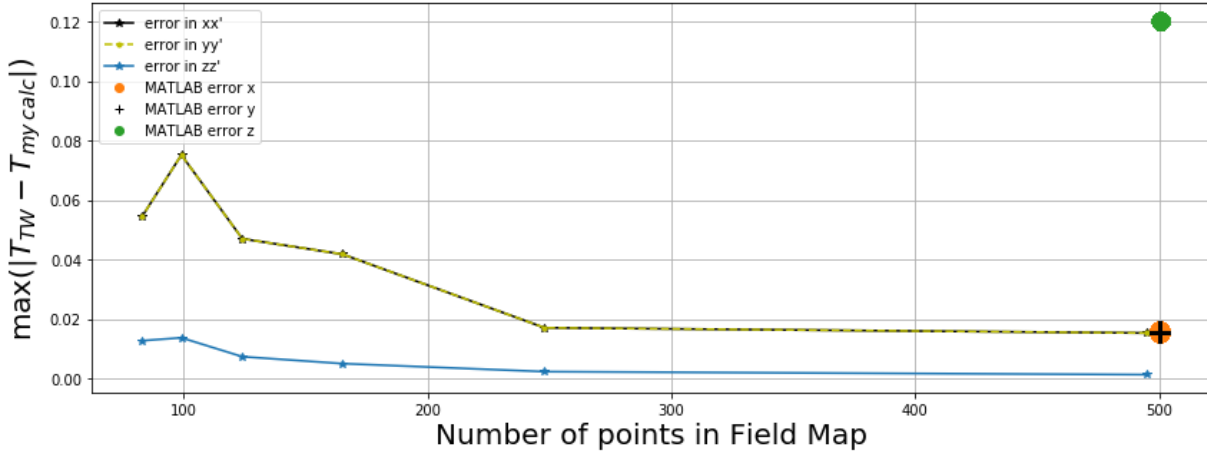
Figure 12: The figure shows the difference between the transfer matrices generated in my program for a simple four-cavity lattice, compared to the matrices generated by TraceWin as a function of number of points in the Field Map of a spoke cavity. The difference is calculated using $max(abs(\mathbf{T}_{\text{TraceWin}} - \mathbf{T}_{\text{my Calc}}))$. The dots correspond to the matrices from the original matlab code.

The error seems to be small, even smaller than the error of the original Matlab Code [17]. This means that this method of constructing the transfer matrices of an accelerator is about as good as TraceWin's method. Note that no structure errors have been taken into account, meaning no coupled elements in the transfer matrices.

3.5.2 Envelope, Twiss beta and phase advance of ESS lattice

All simulations were conducted without the effects of space charge.

Lattice 0 If the nominal lattice is matched without regard to space charge, let's call this *Lattice0*, the nominal envelope according to TraceWin was:
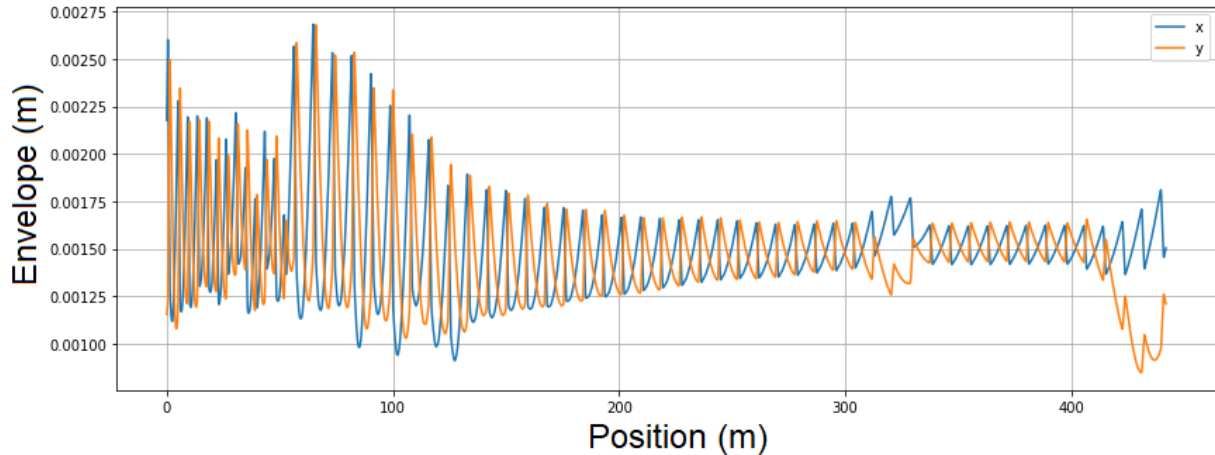
Figure 13: This is the envelope calculated by TraceWin for the nominal Lattice0.

The Twiss β function calculated from TraceWin compared with the Twiss β function calculated from my program for the nominal Lattice0 can be seen in figure 14.

23
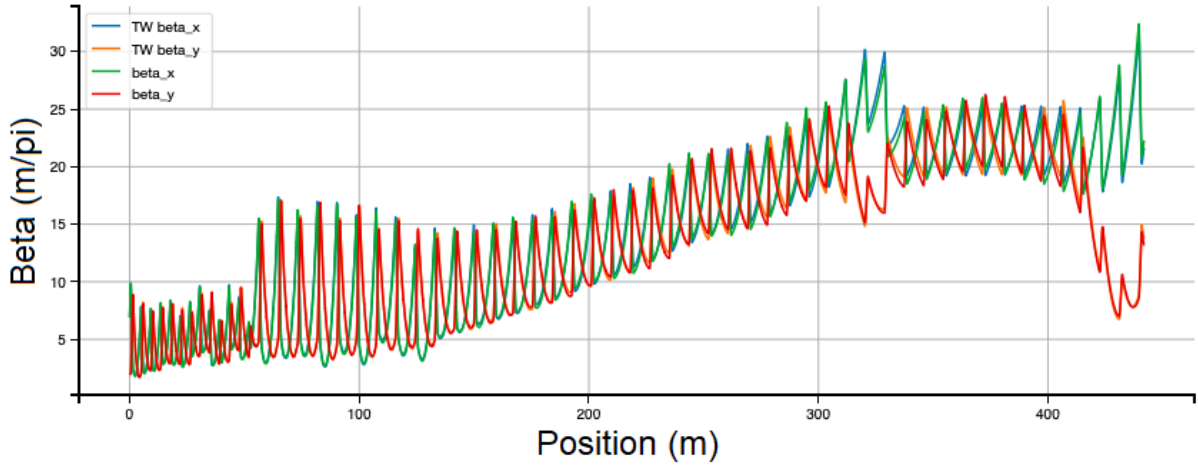
(a)
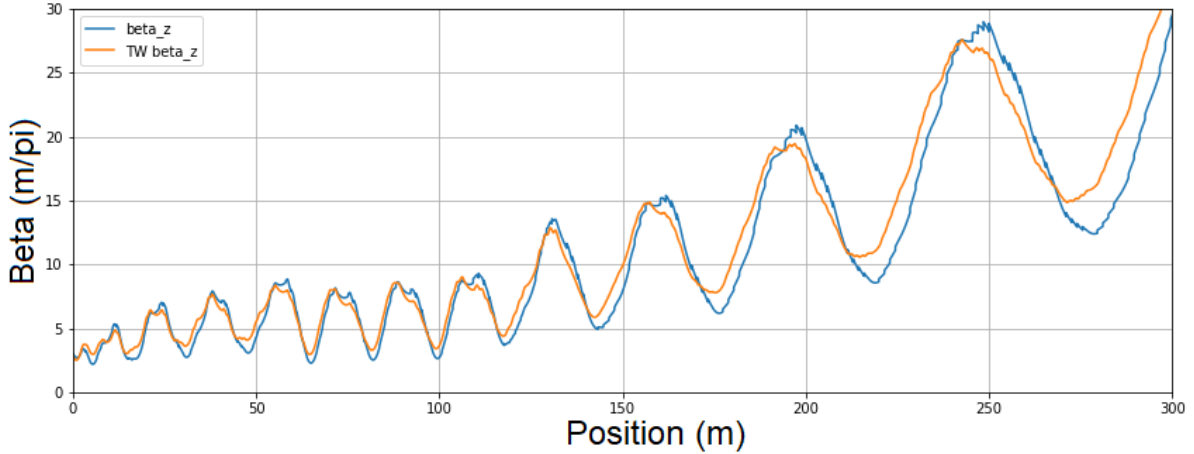
(b)

Figure 14: The figure shows the Twiss beta functions calculated from both TraceWin and my program for *Lattice0*. The transverse calculations are displayed in 14a and the longitudinal in 14b.

Since β_z is not plotted from TraceWin I calculate it from equation (78).

$$\beta_z(z) = 2\frac{\sigma_z^2 \beta_{rel}\gamma_{\mathrm{rel}}^3}{\epsilon_z} \tag{78}$$

The factor $\beta_{\mathrm{rel}}\gamma_{rel}^3$ is the conversion factor from the geometrical emittance, ϵ_z to the normalized emittance, ϵ_{zn} [8]. The same results as TraceWin were reached if the 2 was included in 78, this factor is not analytically derived. The resulting product is used as β_z in the calculations of beam phase advance, see equation (75).

Both the structural and the beam phase advance was calculated and compared to TraceWin. Each point in the graphs coming from my program is the phase advance for each FODO cell, i.e. the phase advance from halfway through a focusing quadrupole to halfway through the next focusing quadrupole.

The phase advance for this lattice was also calculated and the results from both calculations can be seen below. The beam phase advance is presented in figure 15 and the structural phase advance in figure 16.
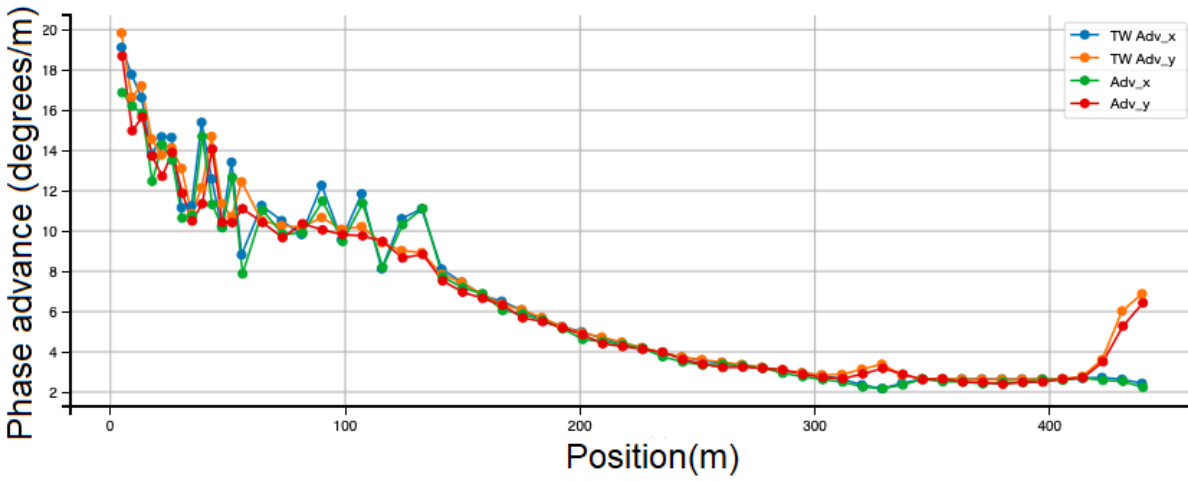
(a)
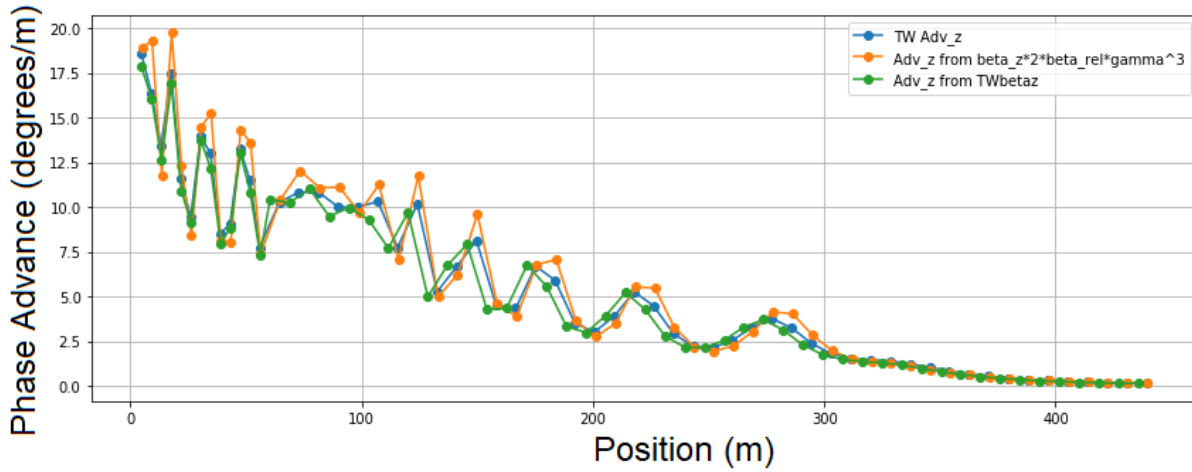
(b)

Figure 15: The graphs show the beam phase advance calculated from TraceWin as well as from my program for *Lattice0*. 15a shows the transverse phase advance and 15b shows the longitudinal phase advance taken straight from TraceWin, calculated from TraceWin β_z and from my $\beta_z * 2 * \beta_{\mathrm{rel}}\gamma^3$.

The similarity between the three curves of longitudinal beam phase advance suggests that the correct β_z was calculated and that the factor $2\beta_{\mathrm{rel}}\gamma^3$ makes my calculated β_z close enough to be used in the retuning routine as accurate data.
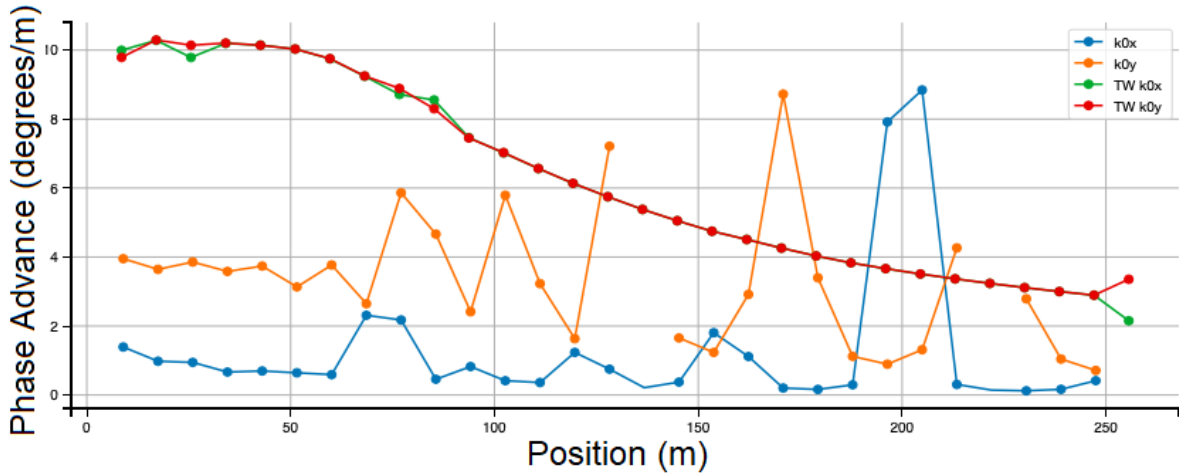
(a)
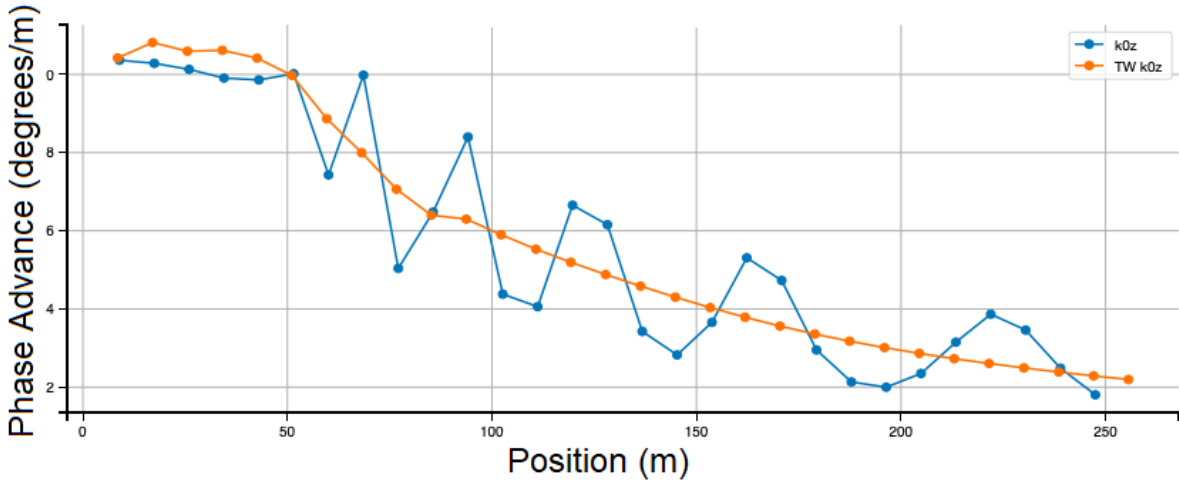
(b)

Figure 16: The graphs show the structural phase advance calculated from TraceWin as well as from my program for *Lattice0*. 16a shows the transverse phase advance and 16b shows the longitudinal phase advance.

The structural phase advance is not the same, which mean that it cannot be assumed to be accurate and therefore not used in the retuning routine. TraceWin defines the structure period in a specific way which is not replicated in my code. For simplicity, I define a structure period to be halfway through a focusing quadrupole to halfway though the next focusing quadrupole.

LatticeSC The ESS Lattice matched with respect to space charge is in this project called *LatticeSC*. The result of calculating Twiss beta and the beam phase advance using my progam and TraceWin can be seen in figure 17. Note that space charge was included in the TraceWin calculations. The difference is quite big for the twiss beta, but the phase advance is not as different.
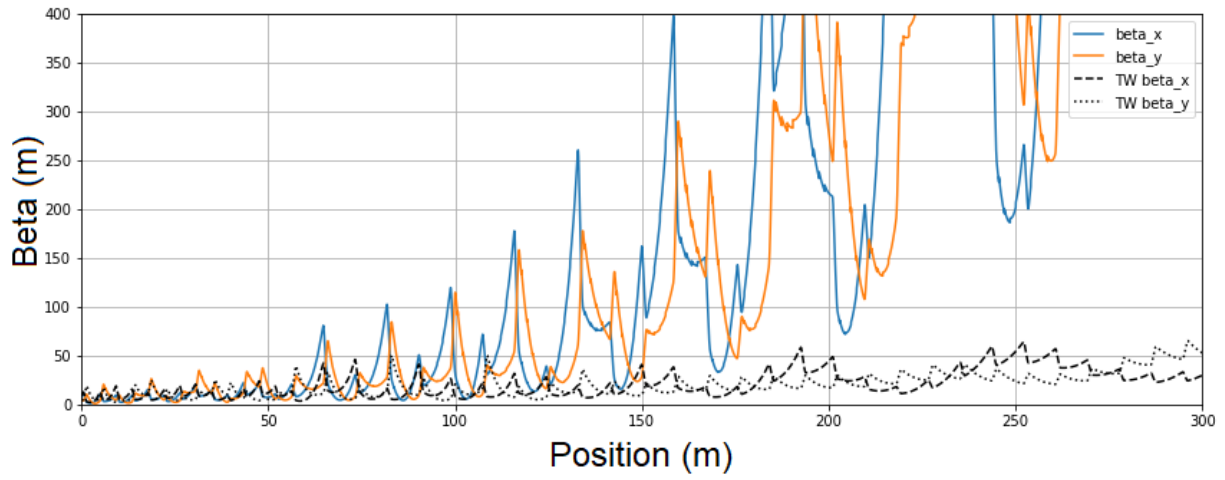
(a)
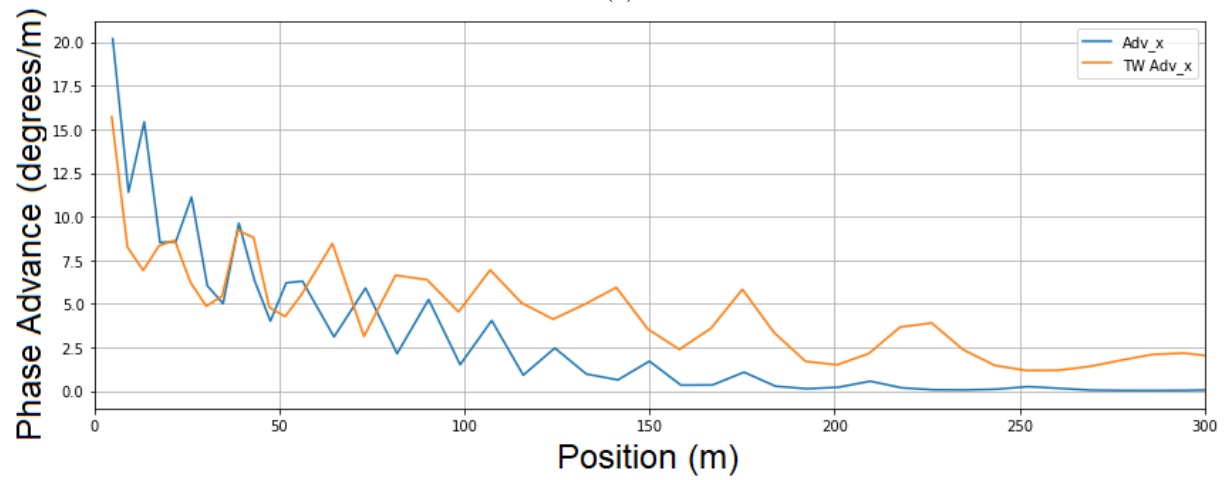
(b)

Figure 17: These graphs are the comparison of the Twiss beta 17a and the beam phase advance 17b between my program and TraceWin, including space charge, for the ESS lattice matched with respect to space charge.

4 Retuning Results

4.1 Retune using only transfer matrices

The goal of the retuning routine is to maintain beam stability. This includes an emittance growth of less than about 10%, a smooth phase advance and not too much oscillations in twiss β. Keeping the beam energy is not a priority, however the final beam energy should not be too low.

All of these graphs in this section were calculated using TraceWin. The two different lattices being retuned are the original ESS lattice, *LatticeSC*, and *Lattice0*. In all beam simulations trough *Lattice0* or any of the retuned versions of *Lattice0*, no space charge was included. This means that the nominal *Lattice0* is matched without respect to the effects of space charge. The effects of space charge were taken into account while matching the original ESS lattice, *LatticeSC*. Space charge was therefore included in the simulations in TraceWin when plotting the retuned results of this lattice. The purpose of this is to determine if a retuning that does not take space charge into account is sufficient.

When one cavity is offline and no retuning is performed the longitudinal emittance increases by several hundred times which can be seen in figure 18. This means that the beam is unstable and is what will be rectified by the retuning routine.
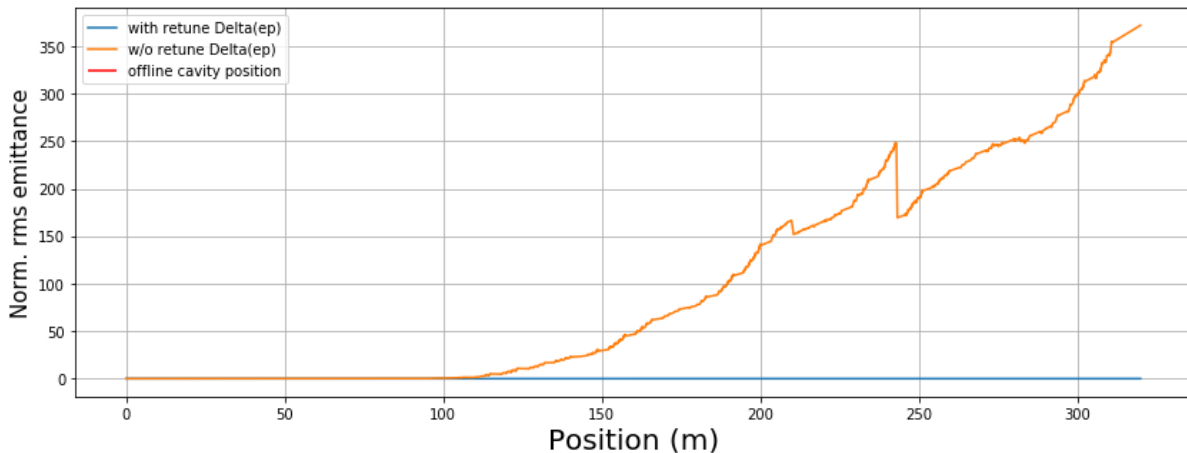
Figure 18: The relative change of the longitudinal rms emittance for *LatticeSC* where cavity SPK #15 is offline and no retuning process has been done.

A beam traveling through a lattice with an offline cavity gains less energy than a beam traveling in the nominal lattice. Table 3 is a summary of the energy the beam achieves in all retuned lattices compared to the nominal lattice with and without the effects for space charge. According to these results, the beam gains less energy if the effects of space charge are included in the beam simulation through a retuned lattice. This is not surprising since the retuning routine does not take the effects of space charge into account. In addition, the beam energy is further from the nominal case the earlier in the machine the offline cavity is located. A lower beam energy is not of major concern as long as the new beam energy is known so that the dipoles steering the beam to the target can be adjusted accordingly. Retaining the beam stability is the most important goal of the retuning.

Table 3: The table is a summary of the final beam energy for the nominal lattice and the retuned lattices where either SPK #15. MBL #30 or HBL #45 is offline. For each case, the energy is calculated with and without the effect of space charge.

Lattice	no space charge	space charge
Nominal	100%	100%
SPK #15	96.7%	96.6 %
MBL #30	97.2%	97.1%
HBL #45	97.6%	97.6%

4.1.1 Failed SPK 15

Lattice0   The results of retuning *Lattice0* when the SPK cavity #15 is offline can be seen below. The beta beat for the retuned lattice can be seen in figure 19. The definition of the beta beat is:

$$\text{beta beat} = \frac{\beta_{i,\text{new}} - \beta_{i,\text{nom}}}{\beta_{i,\text{nom}}} \tag{79}$$
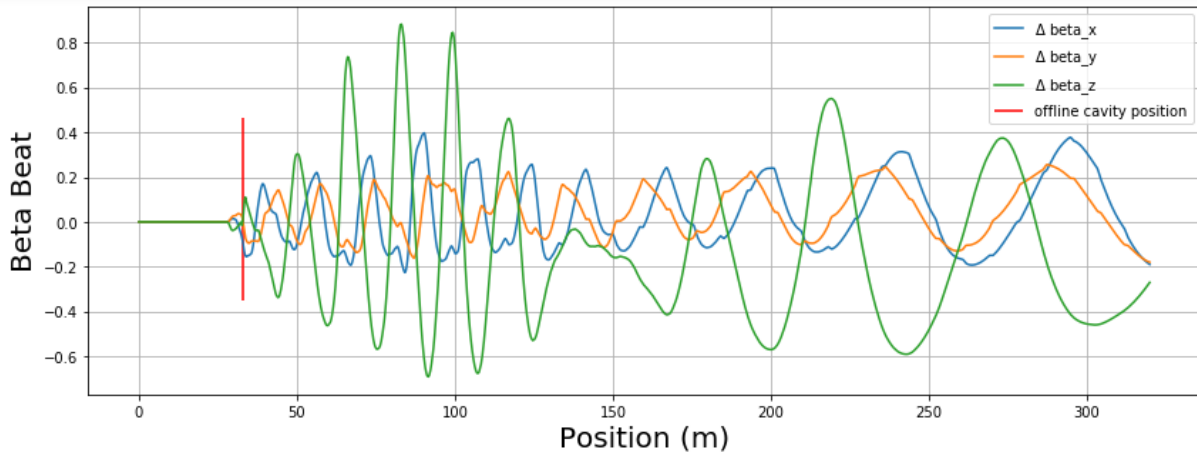
Figure 19: The figure shows the beta beat for the retuned *Lattice0* where SPK #15 is set to be offline. The beta beat in all three dimensions are included in the graph.

The normalized RMS emittance for all three dimensions is displayed in figure 20 for the retuned and the nominal lattice. The new emittance is slightly higher in x and z dimensions in the retuned lattice compared to the nominal case. There appear to be some mismatch around 80m in the longitudinal plane.
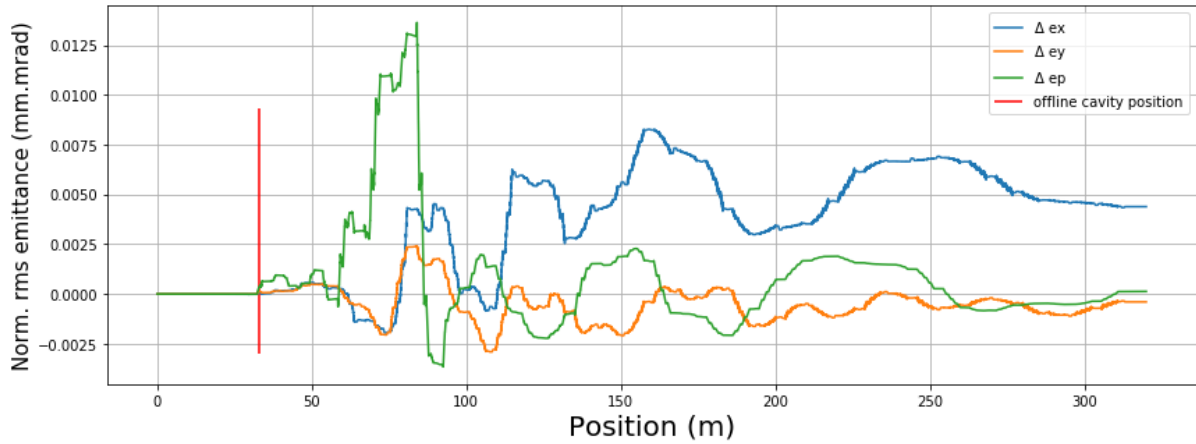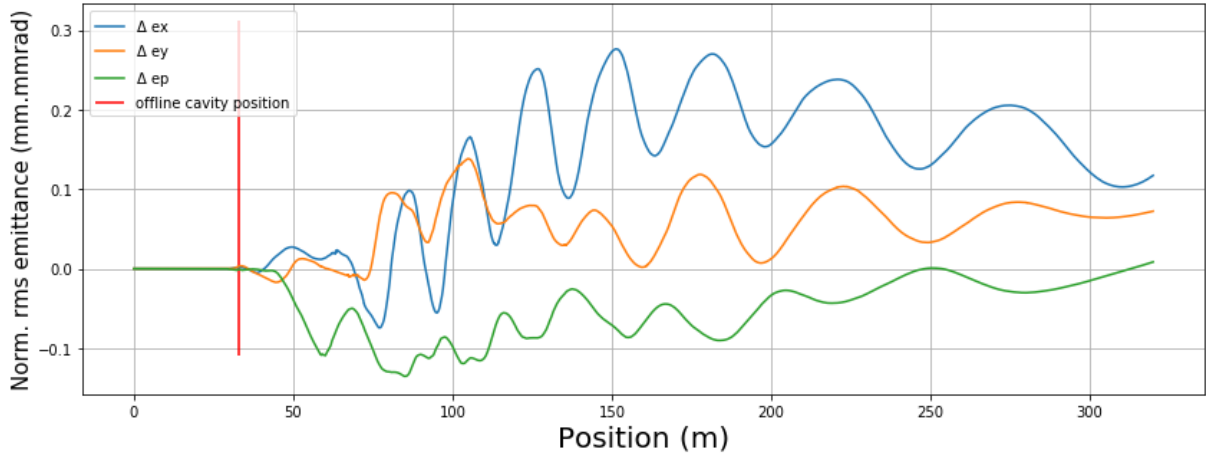
Figure 20: The figure shows the relative change of the normalized RMS emittance in all three dimensions for the retuned *Lattice0* where SPK #15 is set to be offline.

The phase advance was also calculated for the new retuned lattice and compared with the nominal phase advance in *Lattice0*. The change in beam phase advance can be seen in figure 21.
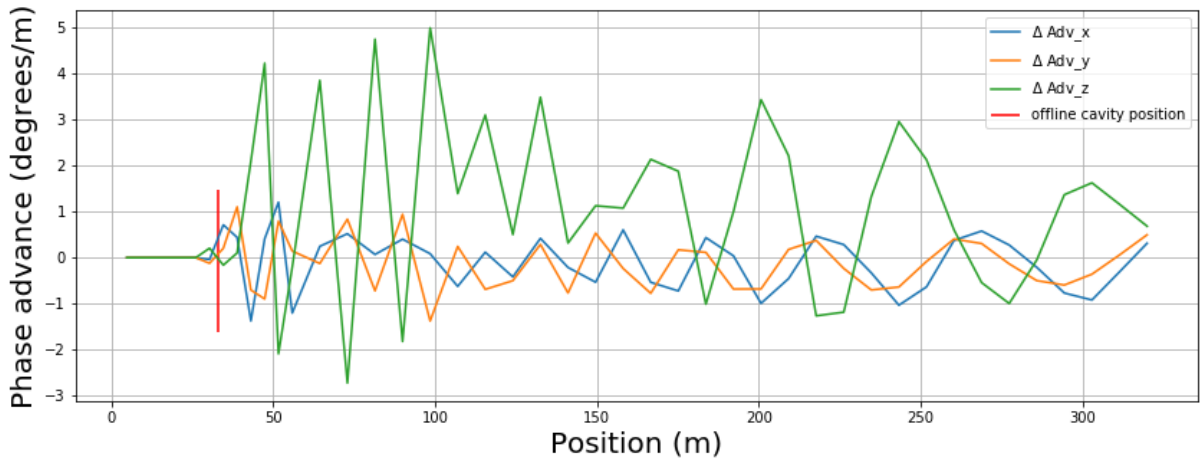
Figure 21: The change in beam phase advance in all three dimensions for the retuned *Lattice0* where SPK #15 is offline compared to the nominal *Lattice0*.

The transverse beam phase advance is very similar for the retuned and nominal lattice, however the longitudinal phase advance differs some, see the green curve in figure 21. There are some more oscillations in the longitudinal phase advance for the retuned lattice, especially around the position of the offline cavity.

The relativistic parameter γ for the retuned and nominal *Lattice0* can be seen in figure 22. The final beam energy is slightly lower in the retuned lattice than in the nominal one, as expected.
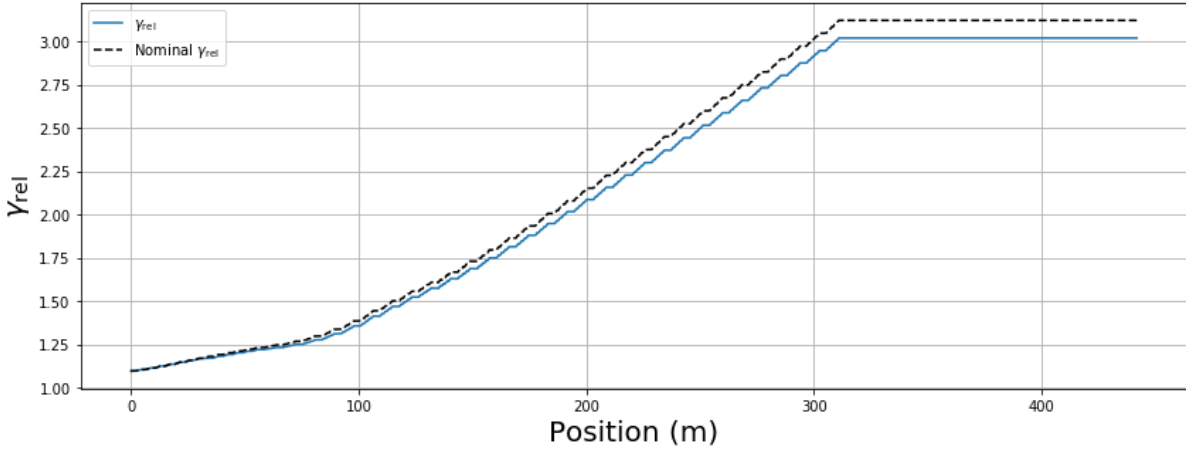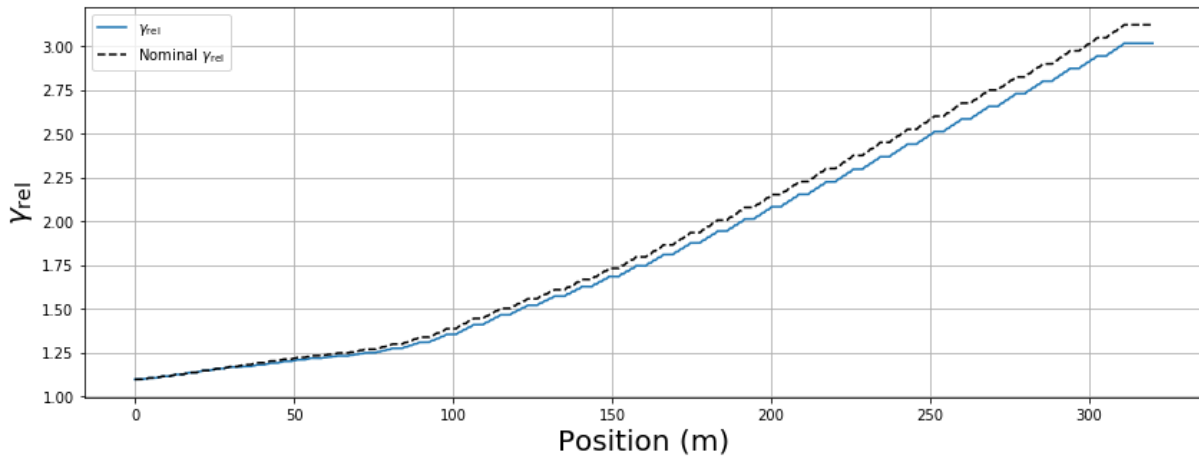
Figure 22: The relativistic γ for the retuned *Lattice0* where SPK #15 is offline and the nominal *Lattice0* is displayed in this figure.

LatticeSC   The results of retuning *LatticeSC* when the SPK cavity #15 is offline can be seen below. The Twiss beta for the retuned lattice compared to the nominal Twiss beta can be seen in figure 23.
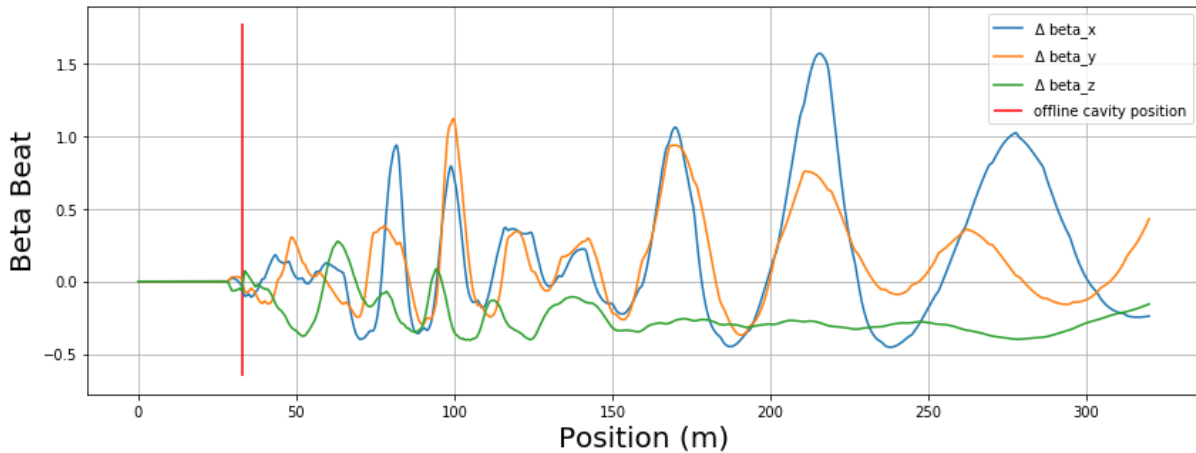
Figure 23: The figure shows the beta beat in all three dimensions for the retuned *LatticeSC* where SPK #15 is set to be offline.

The normalized RMS emittance for all three dimensions is displayed in figure 24 for the retuned and the nominal lattice. The transverse emittance for the retuned lattice is about the same as the nominal emittance, slightly lower for ϵ_y but higher for ϵ_x. ϵ_p is higher than the nominal case.
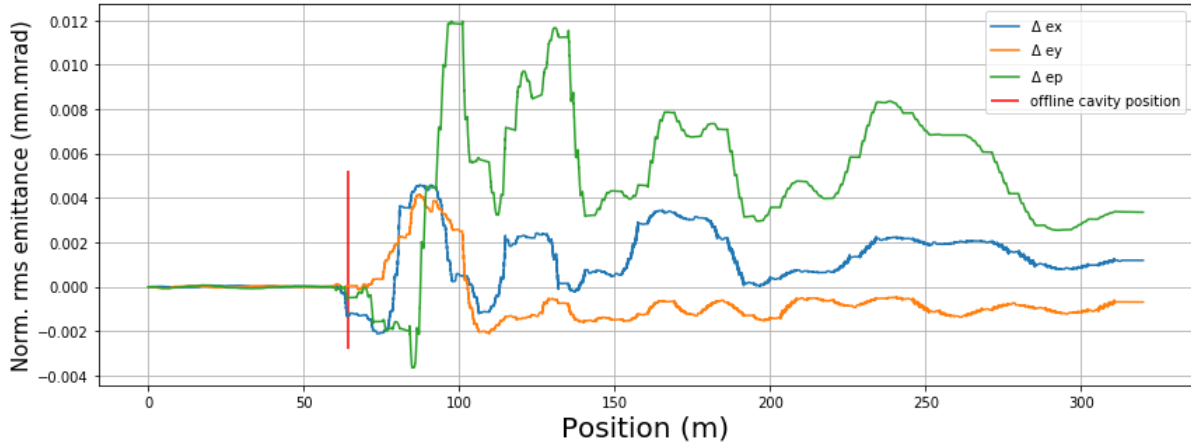
31

Figure 24: The figure shows relative change of the normalized RMS emittance in all three dimensions for the retuned *LatticeSC* where SPK #15 is set to be offline.

The phase advance was also calculated for the new retuned lattice and compared with the nominal phase advance in *LatticeSC*. The change in beam phase advance can be seen in figure 25. The transverse beam phase advance is very similar for the retuned and nominal lattice.
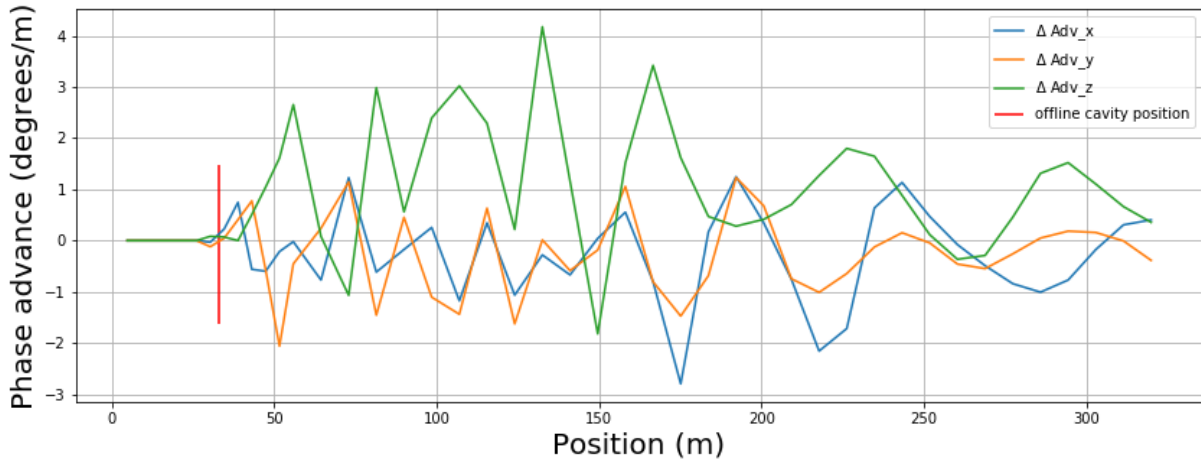
Figure 25: The change in beam phase advance of the retuned *LatticeSC* where SPK #15 is offline can be seen in this figure.

The relativistic parameter γ for the retuned and nominal *LatticeSC* can be seen in figure 26. The final beam energy is slightly lower in the retuned lattice than in the nominal one, as expected. For all tested offline cavities the γ plot is very similar to both figure 22 and figure 26, and will therefore be excluded from the report.

32

Figure 26: The relativistic γ for the retuned *LatticeSC* where SPK #15 is offline and the nominal *Lattice0* is displayed in this figure.

4.1.2 Failed MBL 30

Lattice0 The results of retuning *Lattice0* when the MBL cavity #30 is offline can be seen below. The beta beat for the retuned lattice can be seen in figure 27.
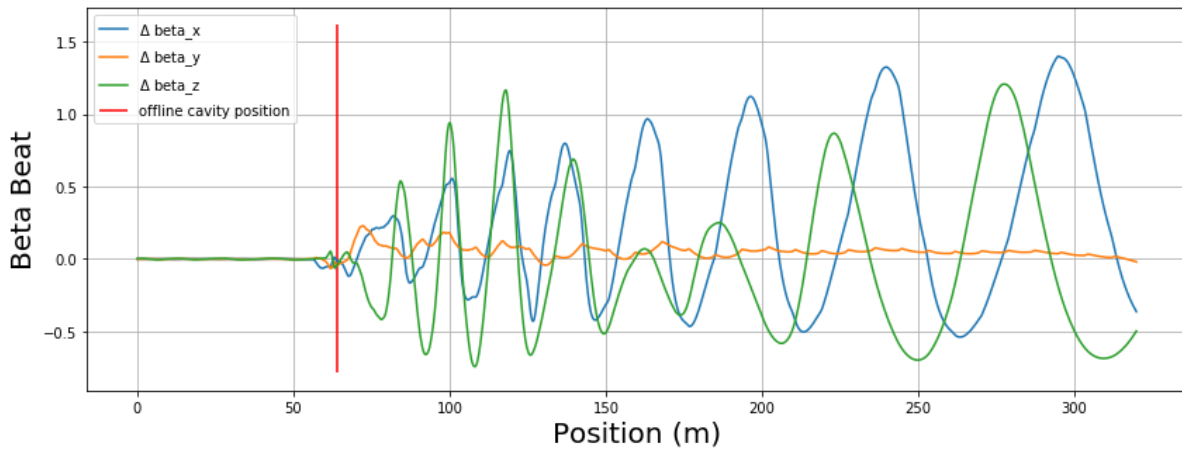
Figure 27: The figure shows the beta beat for the retuned *Lattice0* where MBL #30 is set to be offline.

The normalized RMS emittance for all three dimensions was calculated using TraceWin and can be seen in figure 28 for the retuned and the nominal lattice. The new emittance is slightly higher in all dimensions in the retuned lattice compared to the nominal case, similarly to the SPK #15 retuning.
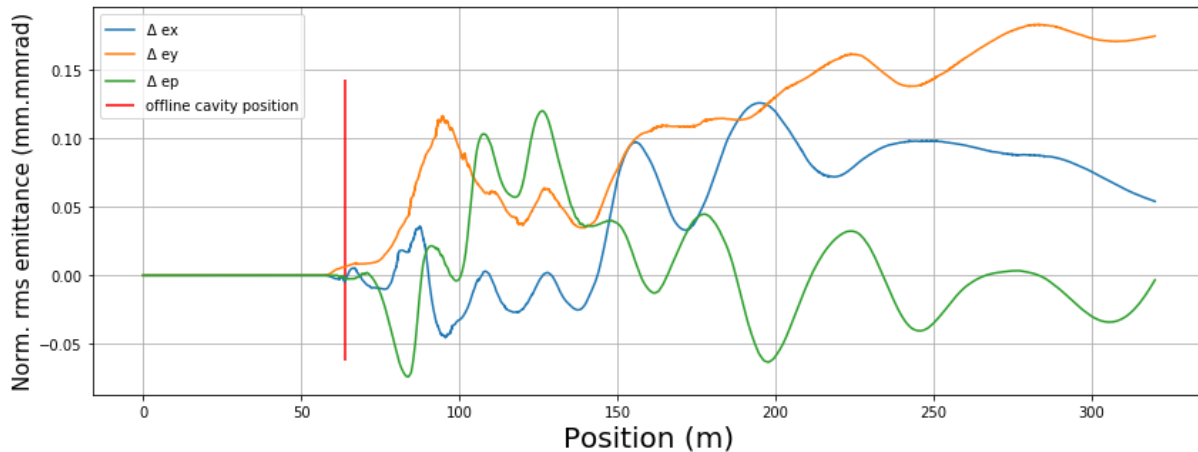
Figure 28: The figure shows the relative change of the normalized RMS emittance in all three dimensions for the retuned *Lattice0* where MBL #30 is set to be offline.

The change of beam phase advance between the new retuned lattice and the nominal *Lattice0* is displayed in figure 29. The transverse beam phase advance is very similar for the retuned and nominal lattice in y phase space. In x phase space and z phase space, the retuned phase advance has slightly higher amplitude and reversed oscillations.
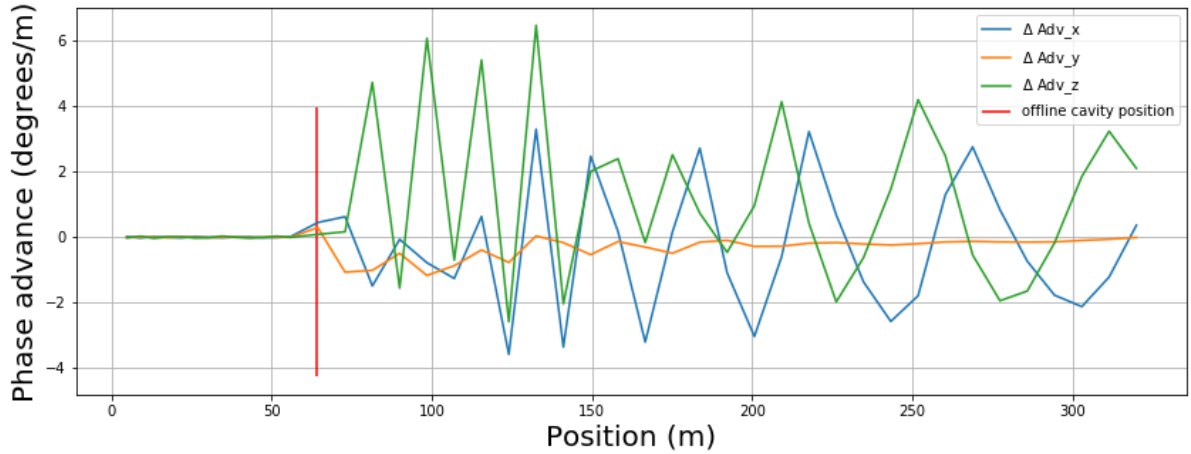
Figure 29: The change of beam phase advance of the retuned *Lattice0* where MBL #30 is offline and the nominal *Lattice0* can be seen in these graphs.

LatticeSC   The results of retuning *LatticeSC* when the MBL cavity #30 is offline can be seen in figure 30. The beta beat for the retuned lattice compared to the nominal Twiss beta can be seen in figure 30.

34
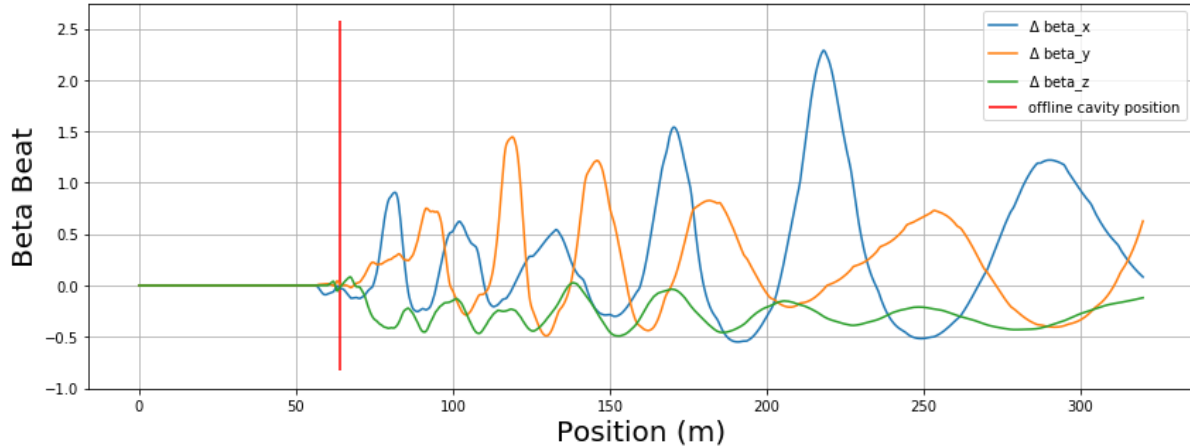
Figure 30: The figure shows the beta beat in all three dimensions for the retuned *LatticeSC* where MBL #30 is set to be offline.

The relative change of the normalized RMS emittance for all three dimensions was also calculated using TraceWin and can be seen in figure 31. The new emittance is about the same as the nominal emittance in the transverse planes. However the longitudinal emittance ϵ_p, is higher for the retuned lattice.

Figure 31: The figure shows the relative change of the normalized RMS emittance in all three dimensions for the retuned *LatticeSC* where MBL #30 is set to be offline.

The change in beam phase advance from the nominal *LatticeSC* to the new retuned lattice where MBL #30 is offline is displayed below. The transverse beam phase advance is quite similar for the retuned and nominal lattice for all dimensions. In longitudinal phase space, the beam phase advance is somewhat higher for the retuned lattice but has a similar shape.
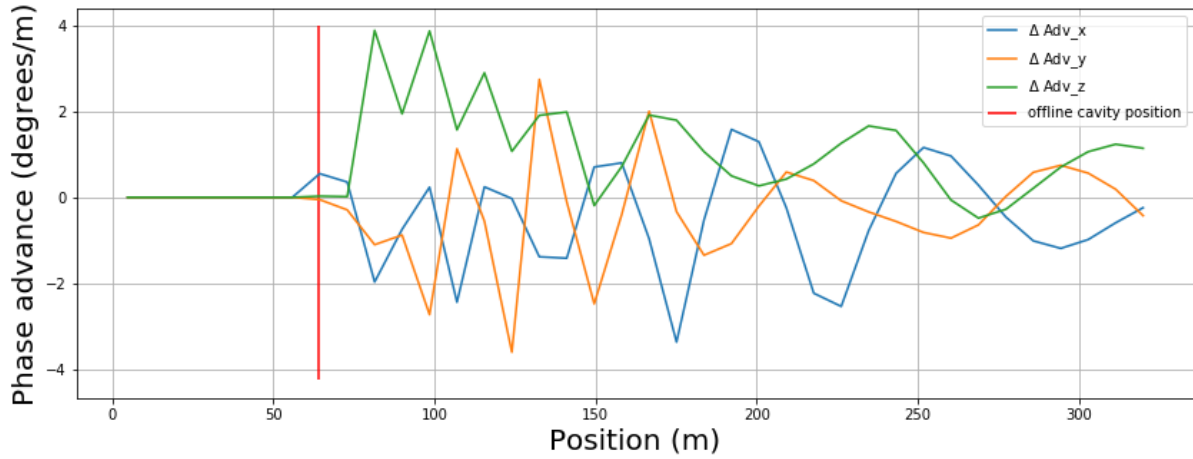
Figure 32: The change in beam phase advance from the nominal *LatticeSC* to the new retuned lattice where MBL #30 can be seen in this figure. The three different graphs correspond to the three dimensions.

4.1.3 Failed HBL 45

Lattice0 The results of retuning *Lattice0* when the HBL cavity #45 is offline can be seen below. The beta beat from the comparison between the retuned and nominal lattice can be seen in figure 33.
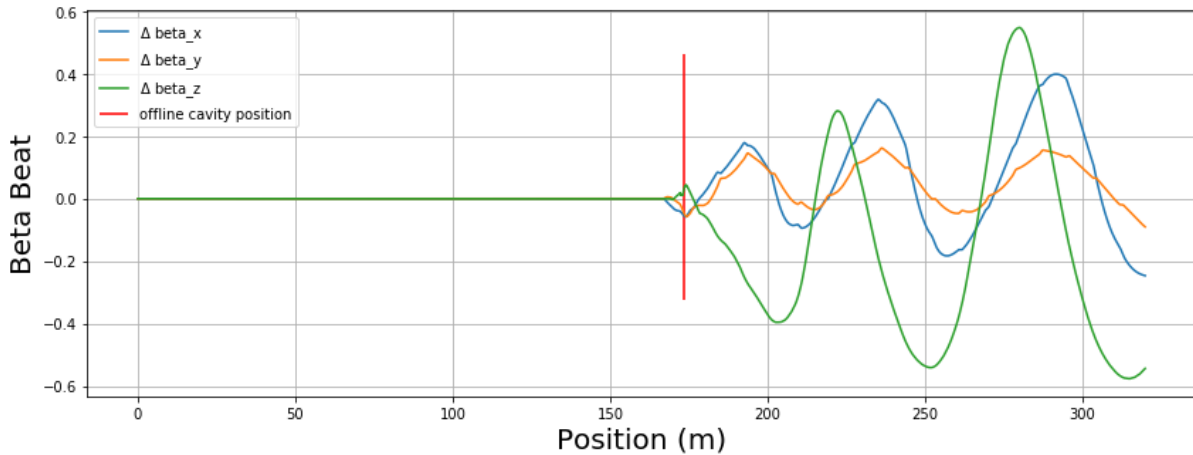

Figure 33: The figure shows the beta beat in all three dimensions for the retuned *Lattice0* where HBL #45 is set to be offline.

The relative change of the normalized RMS emittance for all three dimensions is presented in figure 34. The emittance is higher in the transverse dimensions in the retuned lattice compared to the nominal lattice.
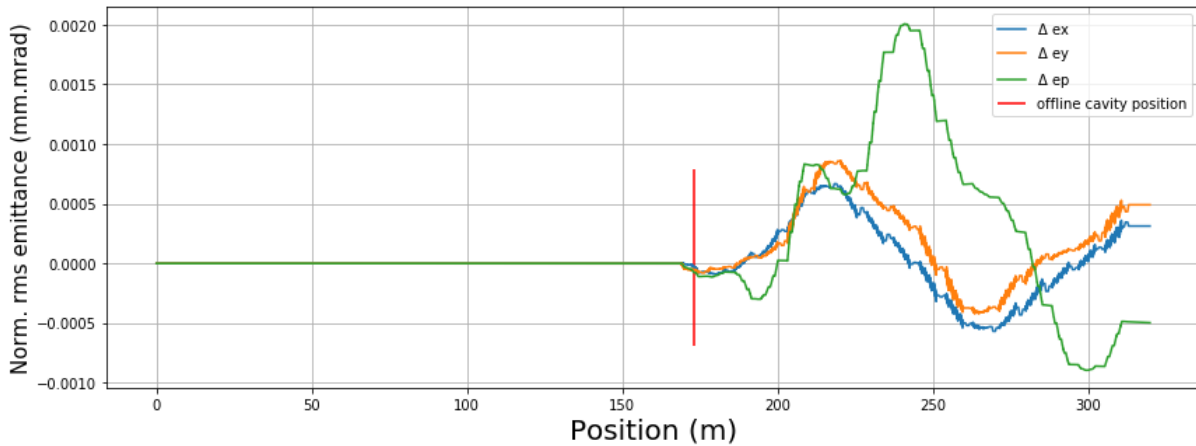
Figure 34: The figure shows the relative change of normalized RMS emittance for the retuned *Lattice0* where HBL #45 is set to be offline.

The change in beam phase advance from the nominal *Lattice0* to the new retuned lattice is displayed below. The transverse beam phase advance for the retuned and nominal lattice are less different than when cavity SPK #15 or cavity MBL #30 is offline.
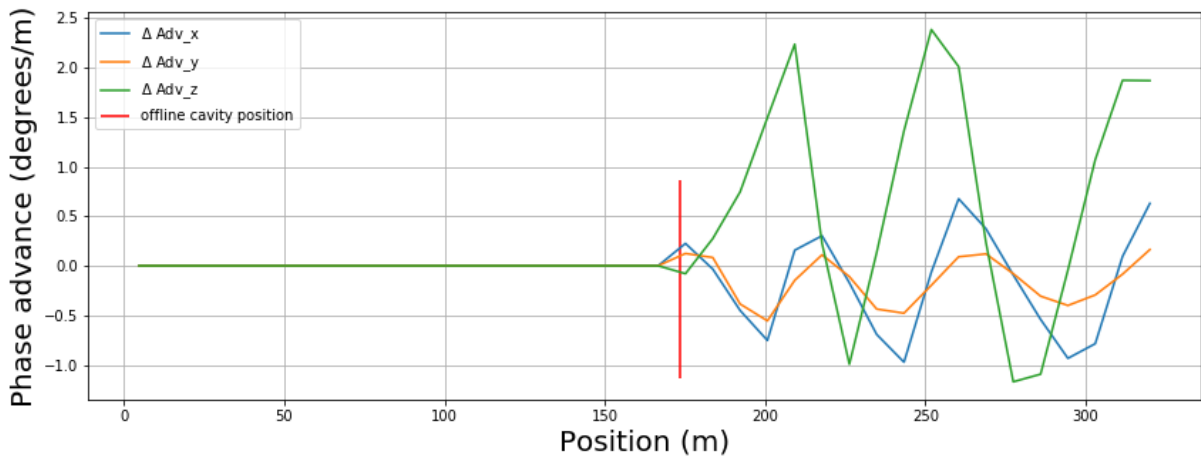

Figure 35: The change in beam phase advance of the retuned *Lattice0* where HBL #45 is offline is displayed in this figure.

LatticeSC The results of retuning *LatticeSC* when the HBL cavity #45 is offline can be seen below. The beta beat for the retuned lattice compared to the nominal Twiss beta can be seen in figure 36.
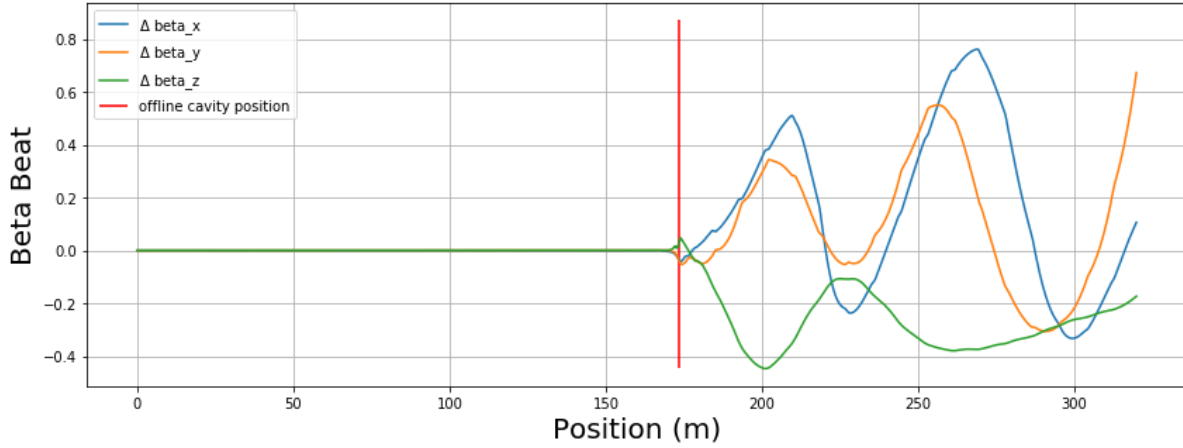
Figure 36: The figure shows the beta beat for the retuned *LatticeSC* where HBL #45 is set to be offline.

The relative change of the normalized RMS emittance for all three dimensions are displayed figure 37 for the retuned and the nominal lattice. The transverse emittance is slightly lower than the nominal case, however the longitudinal emittance is higher.
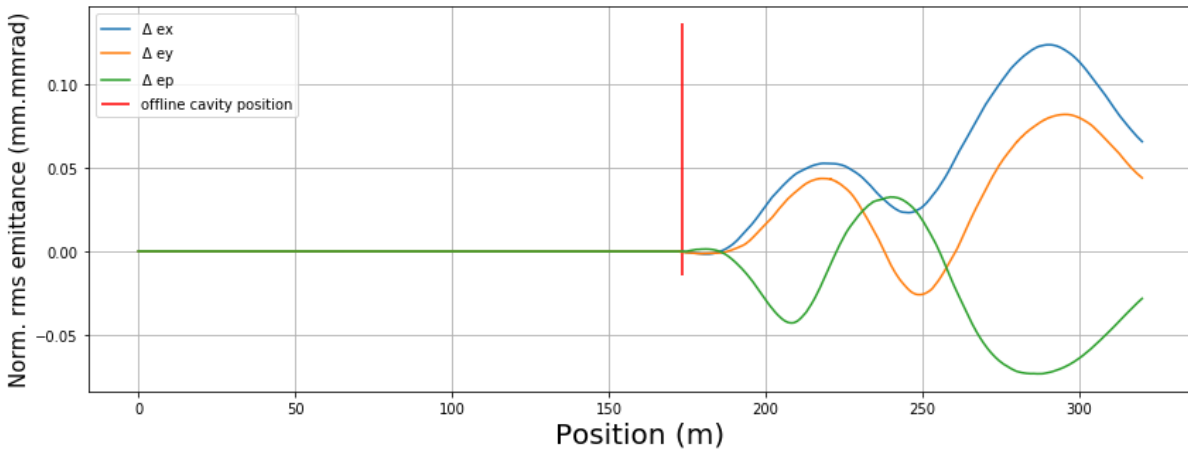

Figure 37: The figure shows the relative change of the normalized RMS emittance for the retuned *LatticeSC* where HBL #45 is set to be offline. The change in all three dimensions are included in the graph.

The change in beam phase advance from the nominal *LatticeSC* to the new retuned lattice is presented in figure 38. This change is quite small.
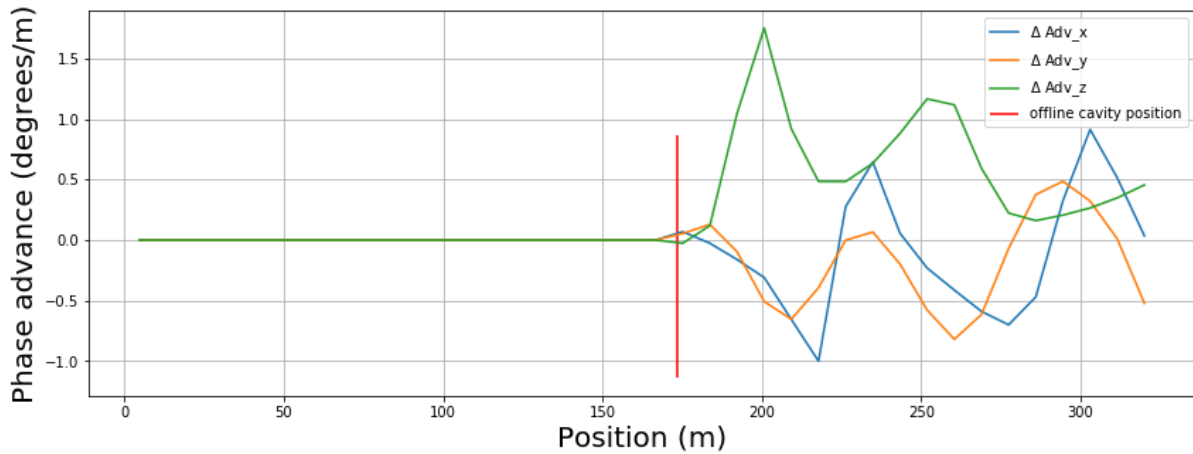
Figure 38: The change of the beam phase advance of from the nominal *LatticeSC* to the new retuned lattice where cavity HBL #45 is offline can be seen in these graphs.

4.2 Retune using both transfer matrices and beam phase advance

If the retuning routine that both optimized the transfer matrix as well as the phase advance were used on the *Lattice0* where again MBL cavity #30 is offline in *Lattice0*. This retuning took **s i g n i f i c a n t l y** more time than the retuning that only optimized the transfer matrix. The beta beat in the *x*-dimension for this lattice can be seen in figure 39 and is very similar to the retuning routine that only optimized the transfer matrices, see figure 27.
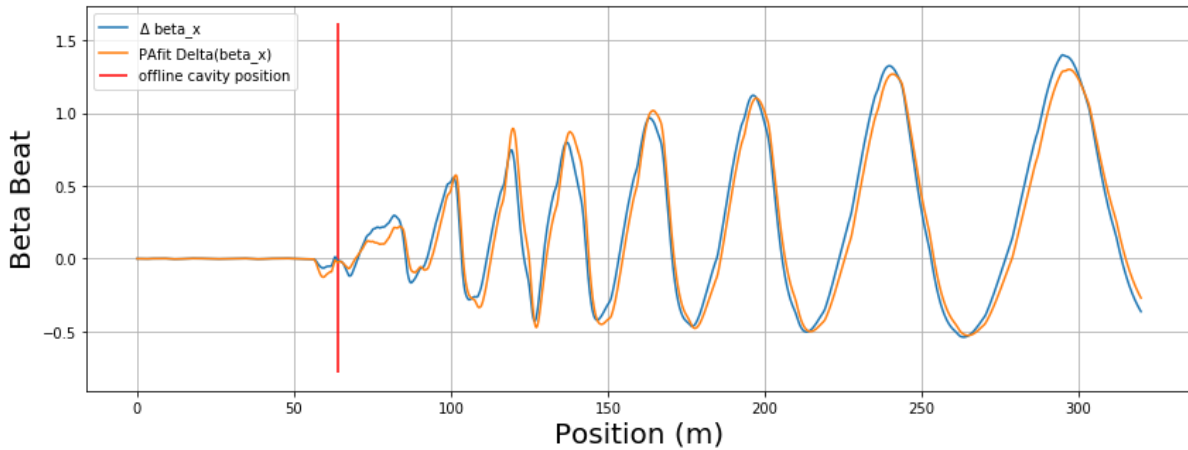

Figure 39: The beta beat in the *x*-dimension for when cavity MBL #30 is offline in *Lattice0* is displayed in this figure for two retuned lattices. The graph named "Δ beta_x" correspond to the beta beat for the lattice retuned using only transfer matrix optimization and the graph named "PAfit Δ beta_x" correspond to the beta beat of the lattice retuned using both transfer matrix optimization as well as beam phase advance optimization.
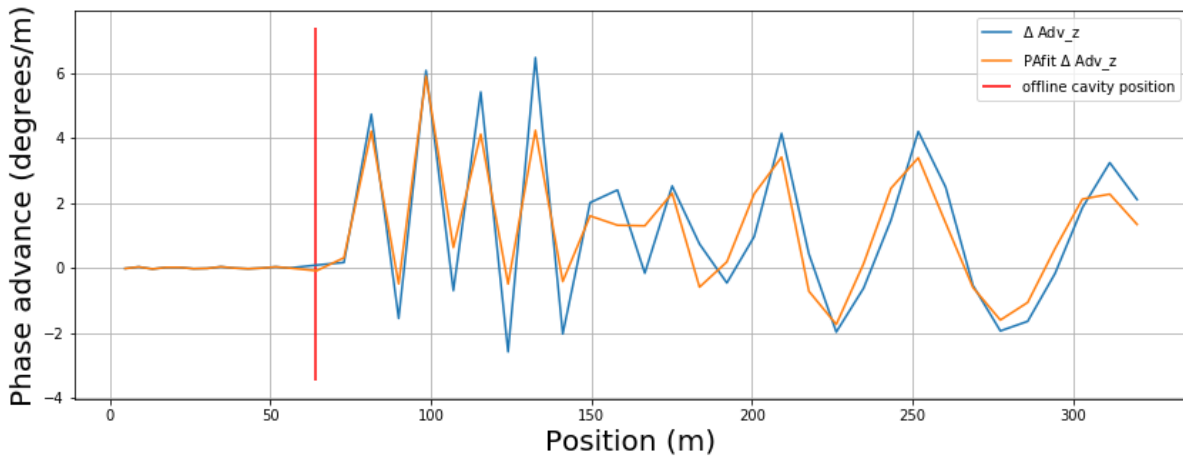
The new change in beam phase advance in figure 40 differs slightly from the retuning results that did not include phase advance optimisation. The beam phase advance was meant to be optimized in a way that made it as smooth as possible. This is done for both the transverse and longitudinal beam phase advance.
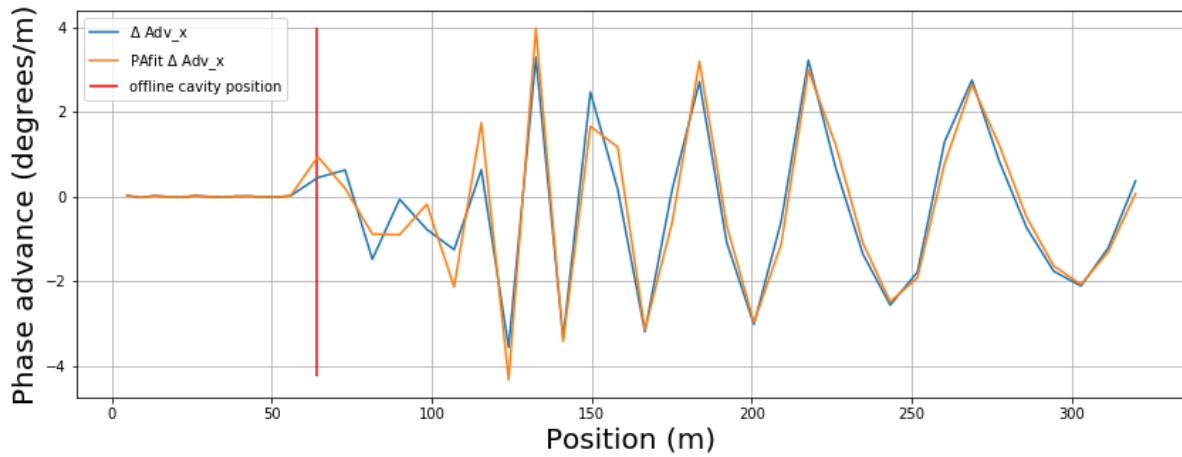
(a)
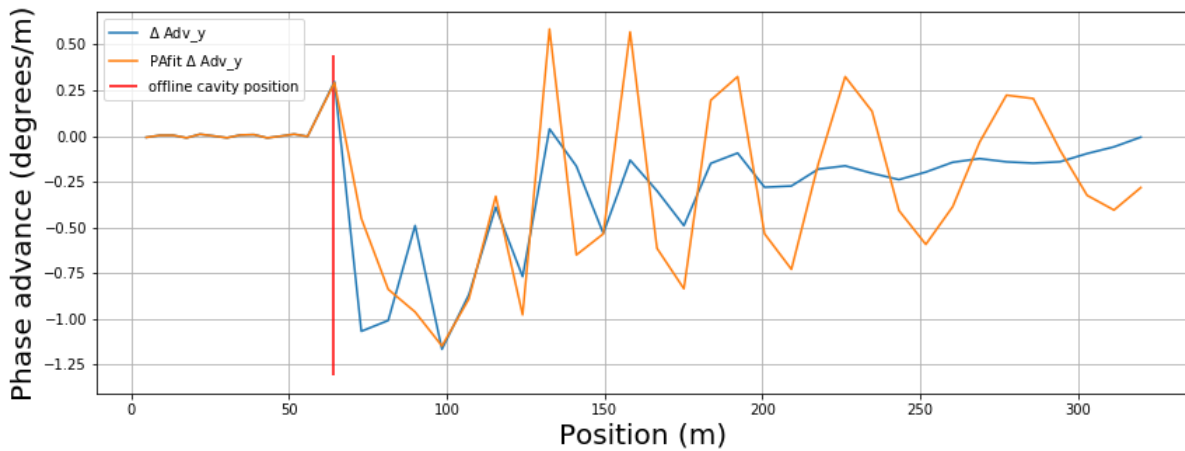
(b)

(c)

Figure 40: The figures show the change beam phase advance for the retuned lattice, where MBL #30 is offline in *Lattice0*. The graphs with labels containing "PAfit" are the results of using a fitness function that optimizes both the beam phase advance as well as the transfer matrix. The results of using only transfer matrix optimisation and the nominal beam phase advance in *Lattice0* are also plotted for comparison. The change of beam phase advance in x is displayed in 40a, the change of beam phase advance in y in 40b and the change in longitudinal beam phase advance in 40c.

40

The longitudinal beam phase advance was somewhat improved by this, however the beam phase advance in y seems to have worsened.

5 Discussion

The difference between the matrices generated by TraceWin and the matrices generated by my calculations can be seen in figure 12. The difference is in the third decimal of the longitudinal matrix elements and is a bit smaller than the difference between TraceWin matrices and the matrices generated by the code from original MATLAB code. The longitudinal plane is more challenging to model accurately without loss of speed. This could account for my code being slower than the previous code. In addition, the number of points in the field map could be reduced to about 200 points/m without loosing matrix accuracy. This might speed up the retuning process. However, this might not be true if more effects are taken in to account while constructing the matrices.

When the effects of space charge were excluded, also in the matching of the nominal lattice, the Twiss β and the phase advance could be calculated from the theoretical derivations presented in the introduction. See the comparison between my calculations and TraceWins calculations in figures 14a and 15. However, my calculations of the longitudinal Twiss β_z fit the TraceWin calculations if my values were multiplied with the factor 2. This suggests that my calculations are accurate without the affects of space charge.

In contrast, when space charge was included in TraceWin using the lattice matched with respect to space charge, my calculations of Twiss β was no longer accurate which can be seen in figure 17a and 17b. Originally, it was thought that this was close enough to be able to do a retuning routine using only transfer matrix optimisation.

Neither of the retuning routines takes space charge effects into account, which raises the question whether it will be sufficient to retune the ESS lattice accurately enough since the Twiss beta could not be calculated as correctly as in TraceWin. Sections 4.1.1-4.1.3 contains the resulting plots of retuning for when either cavity SPK #15, MBL #30 or HBL #45 were offline using only transfer matrix optimization. The amplitude of the beta beat for a failed cavity was slightly lower, which is better, when space charge is not included. To summarize, all retune cases have acceptable beta beat. The beta beats can be seen in figues 19, 23 for the SPK #15 retune, in figures 27 and 30 for the MBL #30 retune and finally in figures 33 and 36 for the HBL #45 retune.

The final emittance growth for both SPK #15 retunes, see figure 20 and 24, is less than 10% which is acceptable. For both the nominal and the retuned cases, there is less emittance growth without space charge. However, the emittance growth of ϵ_p for the retuned *LatticeSC* is still very low. The retuning routine fulfills the requirements concerning emittance for both *Lattice0* and *LatticeSC*. The emittance as a result of the MBL #30 retune is mostly acceptable in both lattices. But the emittance growth in y is about 17% which is higher than desired. Furthermore, the emittance growths of the HBL #45 retune are acceptable.

In the results for the SPK #15 retune, the beam phase advance is better for the *Lattice0* retune than in the *LatticeSC*, see figures 21 and 25. In both retune cases oscillations are present which is not good and is something that should be improved. The desired beam phase advance is decreasing and smooth, meaning no oscillations. For the MBL #30 retune, the *Lattice0* case introduces some oscillations in the beam phase advance that are not there in the nominal case, whereas in the *LatticeSC* case these oscillations actually have a lower amplitude, see figures 29 and 32. It should however be noted that in the *LatticeSC* retune of failed MBL #30 the longitudinal beam phase advance is increasing between 50 and 100 m, see the green curve in figure 32. This is not desirable and can be improved, and it is the reason for the new fitness function to be written. The beam phase advance in the HBL #45 retune is acceptable for both *Lattice0* and *LatticeSC*.

When a cavity is offline the final energy a particle reaches at the end of the accelerator reduces. According to the results presented in table 3, the earlier in the linear accelerator the cavity failure is, the lower energy does the resulting beam have. Additionally, when space charge is included in the simulations the beam

seems to gain a bit less energy than when space charge is not included.

In conclusion, the major issue with the transfer matrix optimisation was that the beam phase advance for the retuned lattices did not fulfill the desired requirements for beam stability. An attempt to correct this was done using the second fitness function as described in section 3.3.

The fitness function designed to improve the beam phase advance was incredibly slow, so slow that it is not an option in its current state. In addition, it did not improve the beam phase advance much, see figure 32. The beta beat was plotted for the new retuned lattice and was very similar to the results of the previous retuned lattice, see figure 39. As stated in the description of the genetic algorithm in section 3.3, the different fitness functions were weighed so that the errors were approximately of the same size. Since very little difference is observed between the results of using only transfer matrix optimisation and added beam phase advance optimisation, the weight of the beam phase advance fitness value should be much higher to make a difference.

Summary and Conclusion   A retuning around an offline accelerating cavity can be made by transfer matrix optimization of a section of the accelerator containing the offline cavity, the four closest functioning cavities and the four closest quadrupoles. This retuning needs information about the accelerator from a lattice file. The information needed is the length of each drift space, the length and gradient of each quadrupole and the length, percentage of maximum power and input phase of each RF cavity. The variables in the transfer matrix optimisation are therefore the quadrupole gradient and the cavities percentage of maximum power and input phase. The resulting retuned lattices did not fulfill all stability requirement.

The process of creating the transfer matrices to be optimized did not include any effects of space charge. To know if this is a reasonable approximation, a lattice matched without the affects of space charge, *Lattice0*, and the original ESS lattice, *LatticeSC*, were used. The Twiss β and beam phase advance can be calculated accurately for *Lattice0* but not for *LatticeSC* using the calculated transfer matrices. However, the retuning of *LatticeSC* was not much worse than the retuning of *Lattice0* which suggests that even without taking the effects of space charge into account, a fairly accurate retuning can be achieved. The major issue is that the beam phase advance for the retuned lattices did not completely fulfill the requirements for beam stability. This is what was attempted to be rectified with the new fitness function to be used in the genetic algorithm that produced the settings for the retuned lattice. However, the results of the new retuning routine was not completely satisfactory since the beam phase advance of the retuned lattice changed very little. In addition, this new fitness function caused the retuning process to be incredibly slow which means that it is not useful as it is.

6   Further work

In order to improve the retuning routine, to keep the beam phase advance decreasing, the new fitness function that optimize the beam phase advance as well as the transfer matrix can be improved to run faster and be weighed more towards this solution characteristic.

Another possible course of action is to include the effect of space charge in calculating the transfer matrices. This can perhaps be done by treating space charge as perturbations in the equations of motions used in this degree project. The genetic algorithm used for the actual retuning would only be based on transfer matrix optimization, but the transfer matrices themselves would include the effects of space charge.

References

[1] R. Garoby *et al.* The european spallation source design. *Phys. Scr.*, 2018. **93** 014001, page 9-14.

[2] M. Eshraqi R. Miyamoto A. Ponton R. de Prisco E. Sargsyan H. Dølrath Thomsen S. Pape-Møller Y. Inntjore Levinsen, H. Danared. European spallation source lattice design status. In *6th International Particle Accelerator Conference*, Richmond, VA, USA, 2015. JACoW Publishing. doi:10.18429/JACoW-IPAC2015-THPF092.

[3] Y. I. Levinsen R. Miyamoto E. Sargsyan A. Karlsson R. De Prisco, M. Eshraqi. Effect of the field maps on the beam dynamics of the ess drift tube linac. In *6th International Particle Accelerator Conference*, Richmond, VA, USA, 2015. JACoW Publishing. doi:10.18429/JACoW-IPAC2015-THPF078.

[4] C. Marrelli C. Martins R.E. Montaño A. Sunesson R. Yogi R. Zeng A. J Johannson M.R.F. Jensen, G. Göransson. High power rf sources for the ess rf systems. In *Proceedings of LINAC2014*, Geneva, Switzerland, 2014.

[5] L. Celona M. Comunian H. Danared R. De Prisco F. Grespan M. Lindroos D. McGinnis R. Miyamoto-S. P. Møller M. Munoz A. Ponton E. Sargsyan H. D. Thomsen M. Eshraqi, I. Bustinduy. The ess linac. In *5th International Particle Accelerator Conference*, Dresden, Germany, 2014. JACoW Publishing. doi:10.18429/JACoW-IPAC2014-THPME043.

[6] K. Wille. *The Physics of Particle Accelerators - an introduction*. Oxford university press, 2000. p. 85-89.

[7] S. Turner, editor. *CERN ACCELERATOR SCHOOL FIFTH GENERAL ACCELERATOR PHYSICS COURSE*, volume Vol. II. CERN, January 1994. page 933.

[8] Didier Uriot. TraceWin Simulation Software, 2019.

[9] S. Werin. *Accelerator technique*. MAX-lab, 2.5th edition, 2003. p. 52.

[10] H. Wiedemann. *Particle Accelerator Physics*. Springer, 3rd edition, 2007. p. 116-122.

[11] S. Y. Lee. *Accelerator Physics*. World Scientific Publishing Co. Pte. Ltd., second edition, 2004. p. 12.

[12] C. Nyberg. *Mekanik, Partikeldynamik*. Liber, second edition, 2014. p. 33.

[13] Ryoichi Miyamoto. personal communication.

[14] T. P. Wangler. *RF Linear Accelerators*. WILEY-VCH, 2nd edition, 2008. p. 214.

[15] M.J. Syphers D.A. Edwards. *An Introduction to the Physics of High Energy Accelerators*. WILEY-VCH, 2004. p. 173-174.

[16] A. Gad. Genetic algorithm implementation in python. `https://www.linkedin.com/pulse/genetic-algorithm-implementation-python-ahmed-gad`, 2018. retrieved: 2020-04-20.

[17] Yuanshuai Qin. Study on key issues in hebt and cavity failure in hppa. unpublished PhD thesis.
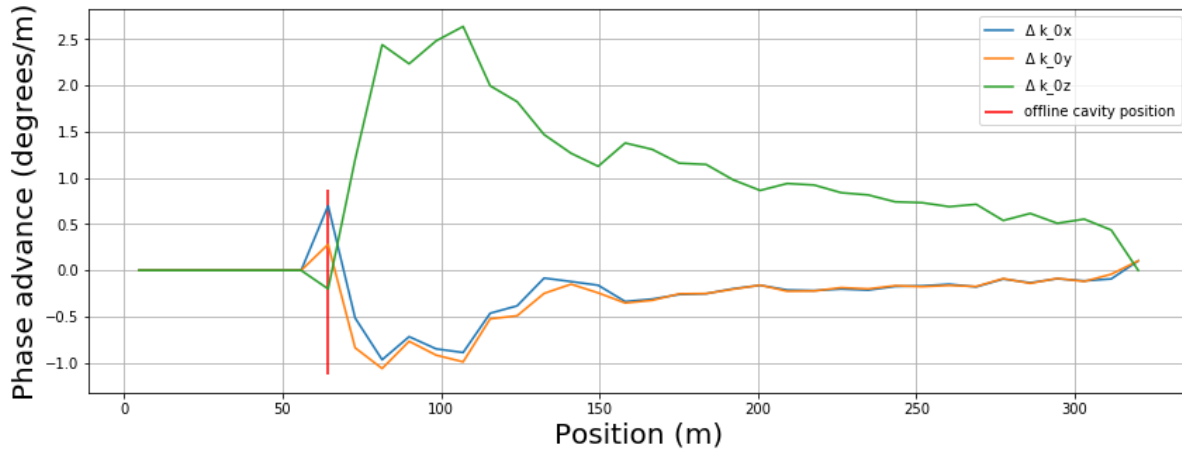
A   Structural Phase advance for retuned lattices

Also the structureal phase advance was calculated for all rematch cases in section 4.1. The change of structural phase advance from the nominal lattice to the retuned lattice can be seen in the figures below.
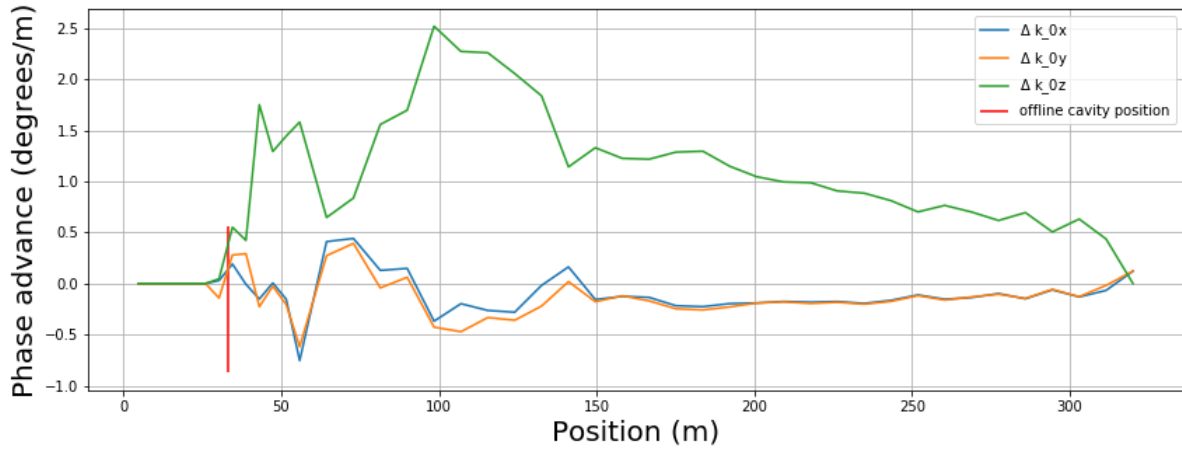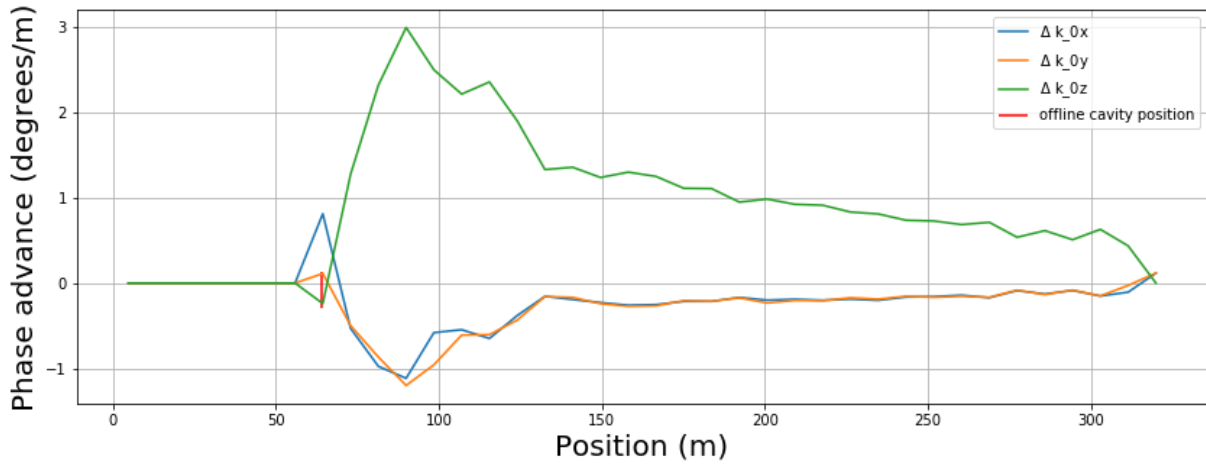
(a) The change in structural phase advance from the nominal *Lattice0* to the retuned lattice where cavity SPK #15 is offline.
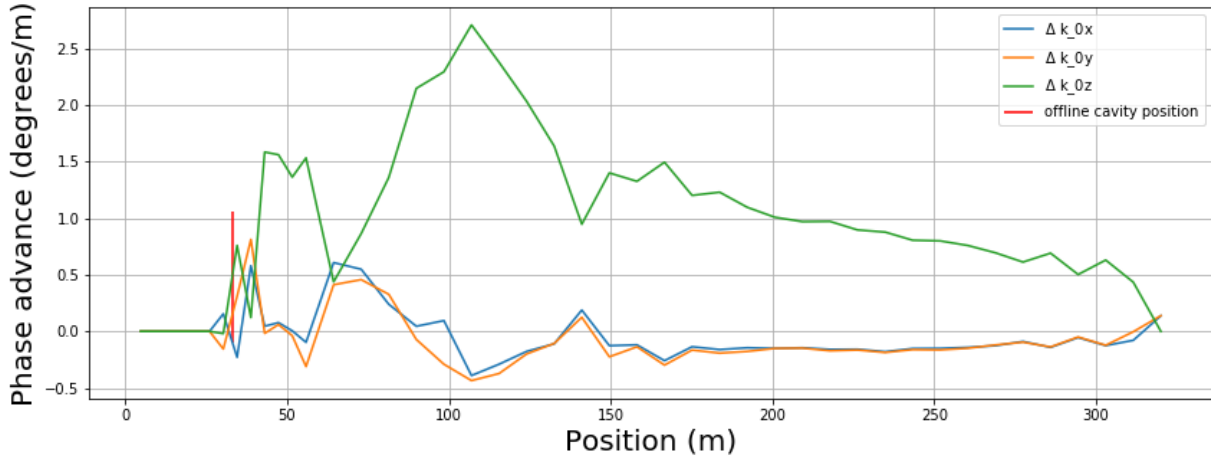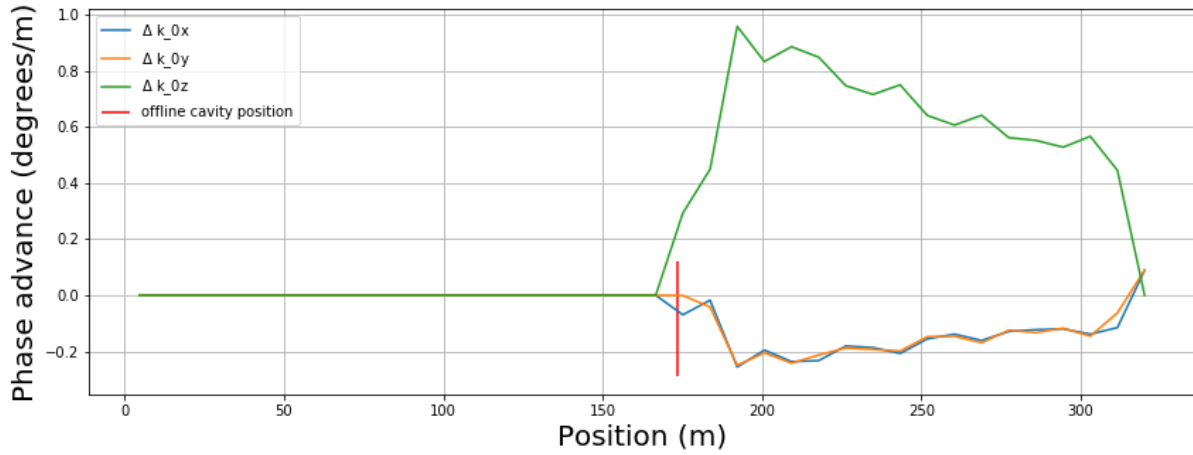

(b) The change in structural phase advance from the nominal *LatticeSC* to the retuned lattice where cavity SPK #15 is offline.
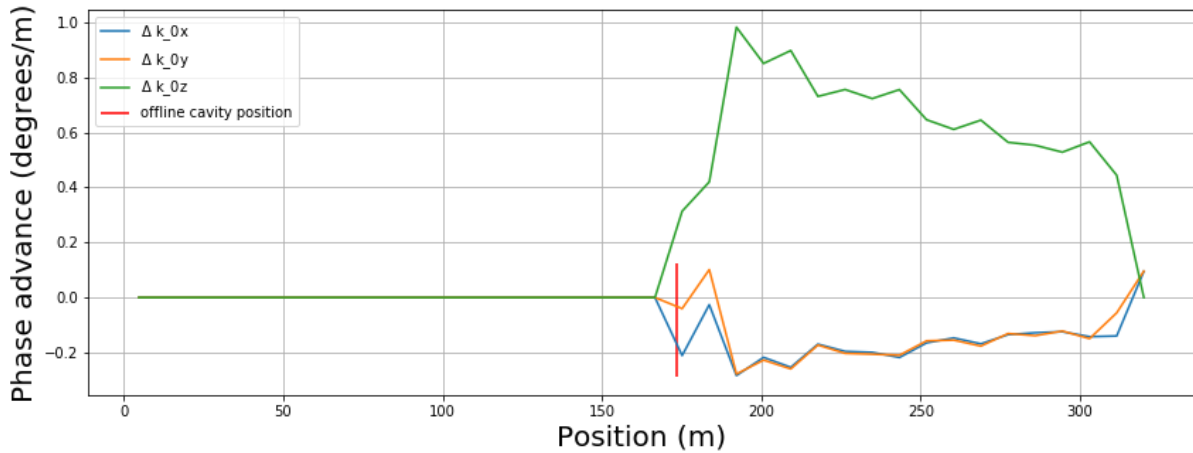

(c) The change in structural phase advance from the nominal *Lattice0* to the retuned lattice where cavity MBL #30 is offline.

(d) The change in structural phase advance from the nominal *LatticeSC* to the retuned lattice where cavity MBL #30 is offline.

(e) The change in structural phase advance from the nominal *Lattice0* to the retuned lattice where cavity HBL #45 is offline.

(f) The change in structural phase advance from the nominal *LatticeSC* to the retuned lattice where cavity HBL #45 is offline.

Figure 41: The change of the structural phase advance for all retuned lattices using transfer matrix optimization.